International Forum on Aeroelasticity and Structural Dynamics
IFASD 2024
17-21 June 2024, The Hague, The Netherlands

MODEL ORDER REDUCTION FOR NONLINEAR AEROELASTIC DYNAMICAL SYSTEMS USING AUTOMATIC DIFFERENTIATION

Declan Clifford[1], **Amir Hossein Modarres Aval**[1], **Andrea Da Ronch**[1]

[1]University of Southampton
Burgess Rd, Southampton SO16 7QF, United Kingdom
dsc1g17@soton.ac.uk
a.h.modarres-aval@soton.ac.uk
a.da-ronch@soton.ac.uk

Keywords: Nonlinear dynamics, reduced order model, aeroelasticity, automatic differentiation

Abstract: An intrusive model order reduction algorithm for nonlinear dynamical systems is presented. Reduced Order Models (ROMs) are constructed using information on the eigenspectrum of the linear dynamical system, projecting a Taylor series expansion of the Full Order Model (FOM) onto a reduced basis of representative eigenvectors. Higher derivatives of the FOM are taken with respect to the ROM coordinate system using source–transformation automatic differentiation. The resultant ROM derivative codes are parameterised with respect to the system properties, thus requiring ROM code generation only once. The algorithm is applied to an aeroelastic pitch–plunge aerofoil with up to cubic structural nonlinearities. The reduced model form sufficiently captures the quadratic and cubic nonlinear dynamics of the full model in response to a range of gust disturbances. Post–flutter limit cycle oscillations are captured using a small subset of modes.

1 INTRODUCTION

Meeting civil aviation sustainability targets requires significant performance improvements of next generation aircraft. Of interest is improving fuel efficiency towards reducing greenhouse, and, other environmentally harmful emissions. One means of achieving this goal is by increasing wing aspect ratio, thus reducing lift–induced drag, and in turn, reducing fuel consumption. These high aspect ratio configurations involve highly flexible lifting surfaces with structural nonlinearities. It is of interest to study the dynamic response of the resultant aeroelastic systems, for example; to verify structural limits are not exceeded in response to excitation; or, to design control laws for gust load alleviation or flutter suppression. Control law design for these highly flexible aeroelastic systems requires sufficiently accurate predictions of the nonlinear dynamics. Use of the full order, nonlinear, coupled fluid–structural system would guarantee accurate prediction of the nonlinear dynamics, but is often computationally intractable for control design. Thus, there exists the motivation for nonlinear Model Order Reduction (MOR), to reduce system size and computational complexity, while retaining the critical dynamical properties of the system.

Ref. [1] formulated a MOR algorithm for application to flexible aircraft control design. The approach uses information of the eigenspectrum from the FOM Jacobian matrix, projecting a Taylor series expansion of the original system onto a representative basis of eigenvectors, thus reducing the state-space dimension, and retaining only critical frequency content. In Ref. [1],

reduced order nonlinearities were approximated via matrix-free Finite-Differencing (FD). In Ref. [2], the same form of MOR technique was modified with Automatic Differentiation (AD) to overcome round-off and/or truncation errors associated with approximating high-order reduced derivatives via FD. This work continues with the work of Ref. [2], now constructing ROMs of nonlinear aeroelastic systems using source–transformation AD. The use of source–transformation AD permits the generation of parametric ROM derivative codes of the FOM source code. These derivative codes are generated once and may be re–evaluated inexpensively for different system parameters.

This work will demonstrate the model reduction algorithm using a two–dimensional aeroelastic aerofoil system with up to cubic nonlinearity in the structure. Compact and parametric reduced order forms of the nonlinear dynamical system are created. This work constitutes an investigation into the form and structure of these reduced models and their capability to predict nonlinear dynamics.

This paper is structured as follows. In Section 2, the general form of the FOM is given. Section 3 continues with a high-level overview of this work's MOR methodology. In Section 4, the aeroelastic system equations of motion are given for an aerofoil section elastically suspended in pitch and plunge. Section 5 continues with an analysis of the dynamics. Nonlinear ROMs are then constructed and their dynamics compared against the nonlinear FOM in Section 6.

2 FULL–ORDER MODEL

The FOM may take the form of a nonlinear dynamical system, expressed here in state–space form as

$$\dot{\boldsymbol{x}} \;=\; \boldsymbol{f}\left(\boldsymbol{x}\left(t\right),\, \boldsymbol{u}\left(t\right)\right) \tag{1}$$

where t denotes the time variable, $\boldsymbol{x}\left(t\right) \in \mathcal{R}^n$ is the system state vector, $\boldsymbol{u}\left(t\right) \in \mathcal{R}^p$ is an input excitation vector, and $\boldsymbol{f} : \mathcal{R}^n \rightarrow \mathcal{R}^n$ is the state evolution function, or nonlinear residual. Here, n represents the state–space dimension and, p, the number of inputs. The system has an initial condition $\boldsymbol{x}\left(0\right) = \boldsymbol{x}_0$, and has an equilibrium point $\boldsymbol{x}_{eq}$ and corresponding $\boldsymbol{u}_{eq}$ such that $\boldsymbol{f}\left(\boldsymbol{x}_{eq},\, \boldsymbol{u}_{eq}\right) = 0$. It is noted that $\boldsymbol{f}$ is assumed to be infinitely differentiable.

Defining $\Delta\boldsymbol{x} = \boldsymbol{x} - \boldsymbol{x}_{eq}$ and $\Delta\boldsymbol{u} = \boldsymbol{u} - \boldsymbol{u}_{eq}$ as the state–vector, and, input excitation vector increments with respect to the equilibrium solution, a Taylor series expansion of the nonlinear residual in Eq. (1) can be expressed as

$$\boldsymbol{f}\left(\boldsymbol{x}\right) \;\approx \boldsymbol{A}_1\Delta\boldsymbol{x} + \boldsymbol{B}\Delta\boldsymbol{u} + \boldsymbol{A}_2\left(\Delta\boldsymbol{x},\, \Delta\boldsymbol{x}\right) \;+ \mathcal{O}\left(\left|\Delta\boldsymbol{x}^3\right|\right), \tag{2}$$

which retains up to second order nonlinearity in the state–vector increment. Here, $\boldsymbol{A}_1 \in \mathcal{R}^{n\times n}$ is the system's Jacobian, or first derivative matrix of $\boldsymbol{f}$, and $\boldsymbol{A}_2 \in \mathcal{R}^n$ is the second order expansion term. $\boldsymbol{B} \in \mathcal{R}^{n\times p}$ is the first derivative of $\boldsymbol{f}$ with respect to the input excitation.

These terms may be defined as follows

$$\boldsymbol{A}_1 \;=\; \left.\frac{\partial \boldsymbol{f}}{\partial \boldsymbol{x}}\right|_{\boldsymbol{x}_{eq}} \tag{3}$$

$$\boldsymbol{A}_2\left(\Delta\boldsymbol{x},\, \Delta\boldsymbol{x}\right) \;=\; \frac{1}{2!}\sum_{r,\,s\,=\,1}^{n} \frac{\partial^2 \boldsymbol{f}}{\partial\, x_r \partial\, x_s}\Delta x_r\, \Delta x_s \tag{4}$$

$$\boldsymbol{B} \;=\; \frac{\partial \boldsymbol{f}}{\partial \boldsymbol{u}} \tag{5}$$

The Taylor expansion of Eq. (2) is used as an approximation of the large–order system of Eq. (1). It is this approximation that is projected onto the reduced basis which is discussed in the subsequent section.

3 MODEL ORDER REDUCTION

The large–order system approximation of Eq. (2) is projected onto a subspace formed by a small number m of eigenvectors of the Jacobian matrix evaluated at the equilibrium point. Given a Jacobian matrix $\boldsymbol{A}_1 \in \mathcal{R}^{n \times n}$, suitable basis vectors are obtained by solving the right and left eigenvalue problems, respectively

$$\boldsymbol{A}_1 \, \boldsymbol{\phi}_r \, = \, \lambda_r \, \boldsymbol{\phi}_r, \qquad \boldsymbol{A}_1^T \, \boldsymbol{\psi}_r \, = \, \bar{\lambda}_r \, \boldsymbol{\psi}_r \quad \text{for } r \, = \, 1, \, \ldots, \, n \tag{6}$$

The eigenvalues of $\boldsymbol{A}_1$ are the same as the eigenvalues of $\boldsymbol{A}_1^T$, whereas the eigenvectors of $\boldsymbol{A}_1$ are different from the eigenvectors of $\boldsymbol{A}_1^T$. If all eigenvalues are distinct, the right and left eigenvectors corresponding to different eigenvalues are biorthogonal ($\bar{\boldsymbol{\psi}}_r^T \, \boldsymbol{\phi}_s \, = \, 0$ for all $r \, \neq \, s$). It is suggested to construct these eigenvectors to satisfy the following biorthogonality conditions

$$\begin{array}{l} \bar{\boldsymbol{\phi}}_r^T \, \boldsymbol{\phi}_r \, = \, 1 \\ \bar{\boldsymbol{\psi}}_r^T \, \boldsymbol{\phi}_r \, = \, 1 \\ \bar{\boldsymbol{\psi}}_r^T \, \bar{\boldsymbol{\phi}}_r \, = \, 0 \end{array} \qquad \text{for } r \, = \, 1, \, \ldots, \, n \tag{7}$$

If these properties are satisfied, then it can be viewed that the projection of the Jacobian matrix on the left and right eigenvectors yields the following relations

$$\bar{\boldsymbol{\psi}}_r^T \, \boldsymbol{A}_1 \, \boldsymbol{\phi}_r \, = \, \lambda_r, \qquad \bar{\boldsymbol{\psi}}_r^T \, \boldsymbol{A}_1 \, \bar{\boldsymbol{\phi}}_r \, = \, 0 \quad \text{for } r \, = \, 1, \, \ldots, \, n \tag{8}$$

A rational choice to extract a small number m of basis vectors is to retain only the slow modes since they are likely to dominate the system dynamics, with the exception of unstable fast modes leading to the instability of the system. The diagonal matrix of eigenvalues, and the right and left modal matrices are written

$$\boldsymbol{\Lambda} \, = \, \begin{bmatrix} \lambda_1 & & \\ & \ddots & \\ & & \lambda_m \end{bmatrix}, \qquad \boldsymbol{\Phi} \, = \, \begin{bmatrix} | & & | \\ \boldsymbol{\phi}_1 & \ldots & \boldsymbol{\phi}_m \\ | & & | \end{bmatrix}, \qquad \boldsymbol{\Psi} \, = \, \begin{bmatrix} | & & | \\ \boldsymbol{\psi}_1 & \ldots & \boldsymbol{\psi}_m \\ | & & | \end{bmatrix} \tag{9}$$

The r–th column of the matrices $\boldsymbol{\Phi}$ and $\boldsymbol{\Psi}$ contains the right and left eigenvector, respectively, associated with the eigenvalue λ_r. These right and left modal matrices contain the desired information about the dynamics of the system.

It is important to note that for a purely real eigenvalue and its corresponding eigenvectors, the biorthogonality conditions cannot be met, as $\boldsymbol{\phi}_r \, = \, \bar{\boldsymbol{\phi}}_r$. This requires the eigenvectors to instead be scaled according to

$$\bar{\psi}_r^T \, \phi_r = \frac{1}{2} \tag{10}$$

which then leads to the relation

$$\bar{\psi}_r^T \, \boldsymbol{A}_1 \, \phi_r = \frac{\lambda_r}{2}. \tag{11}$$

3.1 Linear Reduced Order Model

An approximation of the state vector increment $\Delta \boldsymbol{x}\,(t)$ can be considered with another state vector, constrained to stay in the subspace spanned by the columns of $\boldsymbol{\Phi}$,

$$\Delta \boldsymbol{x} \;\approx\; \boldsymbol{\Phi}\,\boldsymbol{z} \;+\; \bar{\boldsymbol{\Phi}}\,\bar{\boldsymbol{z}} \tag{12}$$

for some $\boldsymbol{z}\,(t) \;\in\; \mathcal{C}^m$. The complex conjugate of $\boldsymbol{z}$ is denoted by $\bar{\boldsymbol{z}}$. Substituting the transformation of coordinates (12) into the large–order system approximation of Eq. (2) while retaining only the linear terms yields an over–determined system of equations with respect to the state vector $\boldsymbol{z}$

$$\boldsymbol{\Phi}\dot{\boldsymbol{z}} \;+\; \bar{\boldsymbol{\Phi}}\dot{\bar{\boldsymbol{z}}} \;=\; \boldsymbol{A}_1\boldsymbol{\Phi}\boldsymbol{z} + \boldsymbol{A}_1\bar{\boldsymbol{\Phi}}\bar{\boldsymbol{z}} \;+\; \boldsymbol{B}\Delta\boldsymbol{u} \tag{13}$$

Pre–multiplication of this equation by $\bar{\boldsymbol{\Psi}}^T$ and then subsequently exploiting the relations of Eq. (7) and Eq. (8) yields a linear ROM, given by

$$\dot{\boldsymbol{z}} \;=\boldsymbol{\Lambda}\boldsymbol{z} \;+\boldsymbol{B}_m\Delta\boldsymbol{u} \tag{14}$$

recalling that $\boldsymbol{\Lambda}$ is a diagonal matrix containing the subset of retained eigenvalues, and defining $\boldsymbol{B}_m \;=\; \bar{\boldsymbol{\Psi}}^T\boldsymbol{B}$.

3.2 Nonlinear Reduced Order Model

Nonlinearities are retained by taking higher order derivatives of $\boldsymbol{f}$ with respect to the reduced state vector variable $\boldsymbol{z}$. For example, the ROM equivalent second order expansion term is given by

$$\begin{aligned}\boldsymbol{A}_2^z\,(\boldsymbol{z},\,\boldsymbol{z}) = \frac{1}{2!}\sum_{r,\,s\,=\,1}^{m}\Bigg(&\left.\frac{\partial^2\,\boldsymbol{f}}{\partial\,z_r\,\partial\,z_s}\right|_{\boldsymbol{x}_{eq}} z_r\,z_s \;+\; \left.\frac{\partial^2\,\boldsymbol{f}}{\partial\,\bar{z}_r\,\partial\,z_s}\right|_{\boldsymbol{x}_{eq}} \bar{z}_r\,z_s \;+\\ &\left.\frac{\partial^2\,\boldsymbol{f}}{\partial\,z_r\,\partial\,\bar{z}_s}\right|_{\boldsymbol{x}_{eq}} z_r\,\bar{z}_s \;+\; \left.\frac{\partial^2\,\boldsymbol{f}}{\partial\,\bar{z}_r\,\partial\,\bar{z}_s}\right|_{\boldsymbol{x}_{eq}} \bar{z}_r\,\bar{z}_s\Bigg)\end{aligned} \tag{15}$$

Then, a nonlinear reduced–order model, retaining up to second order nonlinearity, is written in state–space form as

$$\dot{\boldsymbol{z}} \;=\; \boldsymbol{\Lambda}\boldsymbol{z} \;+\boldsymbol{B}_m\Delta\boldsymbol{u} \;+\bar{\Psi}^T\,\boldsymbol{A}_2^z\,(\boldsymbol{z},\,\boldsymbol{z}) \tag{16}$$

with initial condition $\boldsymbol{z}\,(0) \;=\; \bar{\boldsymbol{\Psi}}^T\,\boldsymbol{x}_0$.

It is noted in Eq. (16), that the ROM second order expansion term $\boldsymbol{A}_2\,(\boldsymbol{z},\,\boldsymbol{z})$ is pre–multiplied by $\bar{\boldsymbol{\Psi}}^T$. This operation may be performed once, prior to time–integration, by pre–multiplying the second order derivatives in Eq. (15) by $\bar{\boldsymbol{\Psi}}^T$. This results in the ROM second order expansion term being constituent of four, second order derivatives, each of which are of dimension $\mathcal{O}\,(m^3)$. Therefore, the ROM nonlinearity is computed also in the dimension of the reduced state vector variable, $\boldsymbol{z}$. Thus, for $m \;\ll\; n$, as assumed initially, the ROM system will provide a computationally inexpensive evaluation of the nonlinearity in comparison with the FOM.

To provide direct comparison with the FOM system approximation of Eq. (2), the equivalent FOM second order expansion term, $\boldsymbol{A}_2\,(\Delta\boldsymbol{x},\,\Delta\boldsymbol{x})$ is constituent of one, second order derivative, of dimension $\mathcal{O}\,(n^3)$. This term is illustrated in the left hand side of Figure 1. The right hand side of Figure 1 shows an illustration of the four ROM second order derivative terms, after pre–multiplication by $\bar{\boldsymbol{\Psi}}^T$.

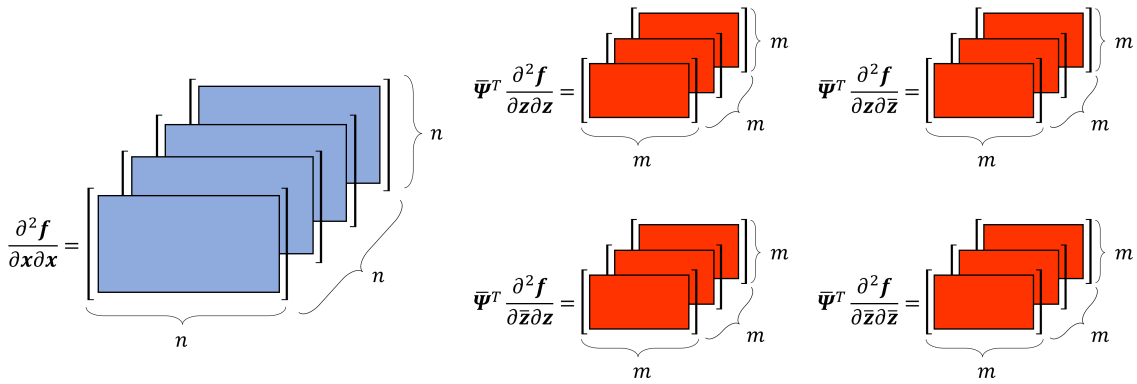

Figure 1: Illustrative comparison of the FOM (left) and ROM (right) second order derivatives, recalling that n is the dimension of the FOM and m, the dimension of the ROM.

3.3 Higher Order Reduced Order Model Derivatives

Formation of the nonlinear ROM requires computing the higher order derivatives with respect to the reduced state vector variable $\boldsymbol{z}$, such as those within Eq. (15). In Refs. [1], [3] and [4], the higher order ROM derivatives are computed using matrix–free finite differencing. Finite–differencing however can suffer from round–off and truncation errors, making the computation of subsequent higher–order derivatives difficult. It is noted in Ref [4], that these difficulties are more significant in the evaluation of the third derivative with finite–differencing, where evaluation of the second derivative is otherwise successful.

In Ref [2], Automatic Differentiation (AD) was used to obtain machine precision accurate derivatives in a computationally efficient manner. AD exploits the fact that a computer code that implements a general function $\boldsymbol{y} = \boldsymbol{f}(\boldsymbol{x})$ can be decomposed into a sequence of elementary function operations. The derivative is then obtained by applying the standard differentiation rules (e.g., product, quotient, and chain rules). This work employs the same technique, using the `ADiGator MATLAB` toolbox [5] for AD. It is noted here that source–transformation AD is used. This allows the formation of ROM derivative codes. These codes need only be generated once, after which, they can be evaluated at a fraction of the generation cost to yield the desired ROM derivative. The advantage of the source–transformation technique is that the ROM derivative codes can be parameterised such that a single code generation is valid across a parameter range. The drawback however comes in that the FOM code must be reasonably simple with respect to the number of operations on the state–vector variable, otherwise the source–transformed ROM derivative codes will become impractically large.

The computation of the higher order ROM derivatives with respect to a complex variable is given in Ref [2]. For completeness, the method is described again here.

To start a concise notation is chosen, denoting the complex variable $z \in \mathbb{C}$ as

$$z = \Re(z) + i\,\Im(z) = z_{Re} + i\,z_{Im} \tag{17}$$

The complex derivatives of a real function, $f : \mathbb{R} \to \mathbb{R}$, with respect to z may be written in the form:

$$\frac{\partial f}{\partial z} = \frac{1}{2}\left(\frac{\partial f}{\partial z_{Re}}\bigg|_{z_{Im}} - i\,\frac{\partial f}{\partial z_{Im}}\bigg|_{z_{Re}} \right) \tag{18}$$

and

$$\frac{\partial f}{\partial \bar{z}} = \frac{1}{2}\left(\frac{\partial f}{\partial z_{Re}}\bigg|_{z_{Im}} + i\,\frac{\partial f}{\partial z_{Im}}\bigg|_{z_{Re}}\right) \tag{19}$$

The calculation of any higher order derivative is facilitated by recursive application of Eqs. (18) and (19). Hereafter, it is implicitly understood that the partial derivative is obtained keeping all other variables constant. For example, second order derivatives with respect to z and $\bar{z}$ are:

$$\frac{\partial^2 f}{\partial z\,\partial z} = \frac{1}{4}\left(\frac{\partial^2 f}{\partial z_{Re}\,\partial z_{Re}} - i\,\frac{\partial^2 f}{\partial z_{Re}\,\partial z_{Im}} - i\frac{\partial^2 f}{\partial z_{Im}\,\partial z_{Re}} - \frac{\partial^2 f}{\partial z_{Im}\,\partial z_{Im}}\right) \tag{20}$$

$$\frac{\partial^2 f}{\partial z\,\partial \bar{z}} = \frac{1}{4}\left(\frac{\partial^2 f}{\partial z_{Re}\,\partial z_{Re}} + i\,\frac{\partial^2 f}{\partial z_{Re}\,\partial z_{Im}} - i\frac{\partial^2 f}{\partial z_{Im}\,\partial z_{Re}} + \frac{\partial^2 f}{\partial z_{Im}\,\partial z_{Im}}\right) \tag{21}$$

$$\frac{\partial^2 f}{\partial \bar{z}\,\partial z} = \frac{1}{4}\left(\frac{\partial^2 f}{\partial z_{Re}\,\partial z_{Re}} - i\,\frac{\partial^2 f}{\partial z_{Re}\,\partial z_{Im}} + i\frac{\partial^2 f}{\partial z_{Im}\,\partial z_{Re}} + \frac{\partial^2 f}{\partial z_{Im}\,\partial z_{Im}}\right) \tag{22}$$

$$\frac{\partial^2 f}{\partial \bar{z}\,\partial \bar{z}} = \frac{1}{4}\left(\frac{\partial^2 f}{\partial z_{Re}\,\partial z_{Re}} + i\,\frac{\partial^2 f}{\partial z_{Re}\,\partial z_{Im}} + i\frac{\partial^2 f}{\partial z_{Im}\,\partial z_{Re}} - \frac{\partial^2 f}{\partial z_{Im}\,\partial z_{Im}}\right) \tag{23}$$

The third and subsequent higher order terms can be obtained similarly via further recursive application of Eqs.(18) and (19).

Prior to the practical application of any AD toolbox, it is noted that that while the system dynamics f is defined for real variables (recall, for example, Eq. (1)), the above derivatives are taken with respect to a complex variable, z. This situation can be dealt with using the transformation of coordinates, Eq. (12).

The higher order terms appearing in the nonlinear reduced–order model are formed by combinations of simple derivatives. For example, the second order term can be expressed as

$$A_2^z(z,\,z) = \frac{\partial^2 f}{\partial z\,\partial z}\,z\,z + \frac{\partial^2 f}{\partial z\,\partial \bar{z}}\,z\,\bar{z} + \frac{\partial^2 f}{\partial \bar{z}\,\partial z}\,\bar{z}\,z + \frac{\partial^2 f}{\partial \bar{z}\,\partial \bar{z}}\,\bar{z}\,\bar{z} \tag{24}$$

and the third order term as

$$\begin{aligned} A_3^z(z,\,z,\,z) = {} & \frac{\partial^3 f}{\partial z\,\partial z\,\partial z}\,z\,z\,z + \frac{\partial^3 f}{\partial z\,\partial z\,\partial \bar{z}}\,z\,z\,\bar{z} + \frac{\partial^3 f}{\partial z\,\partial \bar{z}\,\partial z}\,z\,\bar{z}\,z + \frac{\partial^3 f}{\partial \bar{z}\,\partial z\,\partial z}\,\bar{z}\,z\,z + \\ & \frac{\partial^3 f}{\partial \bar{z}\,\partial z\,\partial \bar{z}}\,\bar{z}\,z\,\bar{z} + \frac{\partial^3 f}{\partial \bar{z}\,\partial \bar{z}\,\partial z}\,\bar{z}\,\bar{z}\,z + \frac{\partial^3 f}{\partial z\,\partial \bar{z}\,\partial \bar{z}}\,z\,\bar{z}\,\bar{z} + \frac{\partial^3 f}{\partial \bar{z}\,\partial \bar{z}\,\partial \bar{z}}\,\bar{z}\,\bar{z}\,\bar{z} \end{aligned} \tag{25}$$

4 AEROELASTIC AEROFOIL SECTION MODEL

This section covers the formulation of the aeroelastic FOM used in this work. Subsections cover in order, the structural system, fluid system, and coupled fluid–structural aeroelastic system.

4.1 Structural System

The elastically suspended 2–Degree of Freedom (2–DOF) structural system is as defined in Figure 2. Plunge deflection is denoted by h and pitch deflection denoted by θ, with h and θ defined by convention as positive downwards and clockwise respectively. The pitch and plunge degrees of freedom are both elastically suspended in pitch and plunge, with the plunge restoring force denoted by $\tilde{K}_h(h)$, and the pitch restoring moment denoted by $\tilde{K}_\theta(\theta)$.

The aerofoil has a chord of length c and semi–chord b. a_h denotes the distance between the mid–chord and elastic axis non–dimensionalised by b and x_θ the distance between the elastic axis and centre of mass non–dimensionalised by b. The aerofoil has mass m, a polar moment of inertia about the $1/4$ chord per unit length I_θ, and, static mass moment S_θ, where $S_\theta = mbx_\theta$.

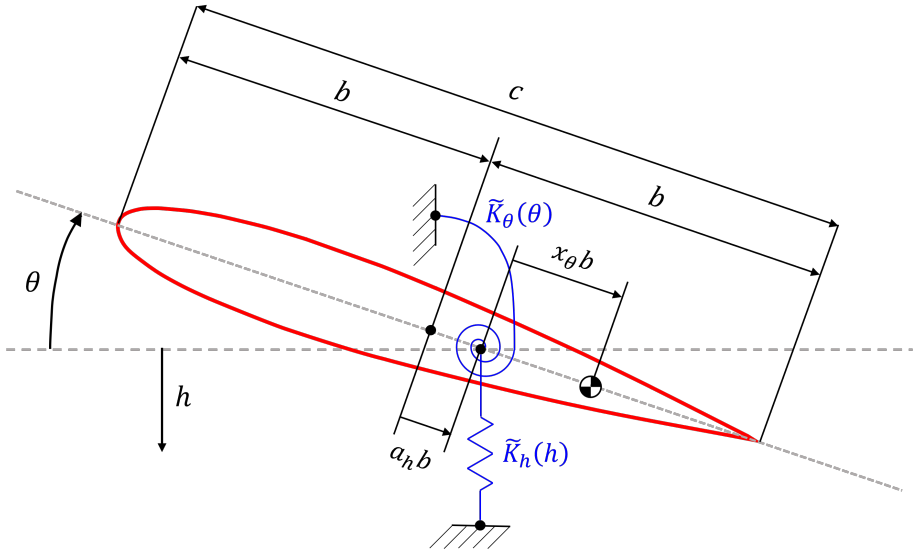

Figure 2: 2–DOF aerofoil structural system

The equations of motion of the structural system may be derived from the Lagrange equations, given by

$$\frac{d}{dt}\left(\frac{\partial \mathcal{L}}{\partial \dot{q}_i}\right) - \frac{\partial \mathcal{L}}{\partial\, q_i} = Q_i \tag{26}$$

where $\mathcal{L}$ is the Lagrangian – defined as the total kinetic energy of the system minus the total potential energy of the system, q_i is a generalised coordinate and Q_i is a generalised force, with the subscript i, denoting in no particular order, the degree of freedom considered. The derivation of the structural system via the Lagrange equations can be found in full in Ref. [6].

The derived equations of motion of the structural system may then be expressed as

$$m\ddot{h} + S_\theta\ddot{\theta} + \tilde{K}_h(h) = Q_h \tag{27a}$$

$$S_\theta\ddot{h} + I_\theta\ddot{\theta} + \tilde{K}_\theta(\theta) = Q_\theta. \tag{27b}$$

where Q_h and Q_θ are the generalised aerodynamic forces in plunge and pitch respectively.

4.1.1 Structural Nonlinearities

Nonlinearity is introduced to the structural system through the plunge and pitch degree of freedom springs. The restoring force and moment of the plunge and pitch springs are defined respectively as

$$\tilde{K}_h(h) = m\omega_h^2\, h\, \tilde{P}_h(h) \tag{28a}$$

$$\tilde{K}_\theta(\theta) = I_\theta \omega_\theta^2 \, \theta \, \tilde{P}_\theta(\theta) \tag{28b}$$

where ω_h and ω_θ are the decoupled frequencies of plunge and pitch respectively. $\tilde{P}_h$ and $\tilde{P}_\theta$ are nonlinear functions which are used to add quadratic and cubic nonlinearities. These terms are defined as

$$\tilde{P}_h(h) = \beta_{h1} + \beta_{h2} \, h + \beta_{h3} \, h^2 \tag{29a}$$

$$\tilde{P}_\theta(\theta) = \beta_{\theta 1} + \beta_{\theta 2} \, \theta + \beta_{\theta 3} \, \theta^2. \tag{29b}$$

Quadratic nonlinearities may be introduced through the parameters β_{h2} and $\beta_{\theta 2}$. Cubic nonlinearities are similarly introduced through the parameters β_{h3} and $\beta_{\theta 3}$.

Structural nonlinearities of this form have been covered extensively in Ref. [7], where it is noted for example that thin lifting surfaces being twisted may be modelled with a cubic hardening spring which becomes stiffer as twist angle increases. It is noted also that buckling can be modelled with the opposite spring softening effect, which can be similarly obtained with a cubic parameter. In Ref. [8] a flutter study was performed considering these hardening and softening structural nonlinearities. It was seen in Ref. [8] that for a system with a softening structural nonlinearity (i.e. a negative cubic term), flutter would occur at a point before it would occur in the equivalent linear dynamical system. This is due to the destabilising effect of the softening nonlinearity, where the restoring force decreases for larger displacement ranges in comparison with the linear system. For the system in Ref. [8] with a cubic hardening structural nonlinearity (i.e. a positive cubic term), it was found that divergent flutter would not occur, with the dynamics instead settling into stable limit cycle oscillations. This work further introduces quadratic parameters to the structural nonlinearity. This is done with the intention of increasing the mathematical complexity of the model, and not necessarily to capture a specific physical phenomenon.

The parameters used in this work may be assumed as those given in Table 1, unless specified otherwise.

Table 1: Pitch and plunge polynomial parameters

Plunge Parameters	Pitch Parameters
$\beta_{h1} = 1.0000$	$\beta_{\theta 1} = 1.0000$
$\beta_{h2} = 0.1500$	$\beta_{\theta 2} = -5.0000$
$\beta_{h3} = 0.0065$	$\beta_{\theta 3} = 8.0000$

The product of the nonlinear functions with their corresponding displacements are evaluated over displacement ranges and shown in Figure 3. The left Figure shows the resultant plunge polynomial and the right Figure shows the resultant pitch polynomial. The line denoted as "Linear" has terms associated with the second and third order nonlinearities set to 0. The line denoted as "Nonlinear" uses the parameters as specified in Table. 1.

It is seen in Figure 3 that for the positive and negative ranges of plunge and pitch displacement, the restoring force and restoring moment will harden or soften. For example, in terms of plunge displacement, in the positive direction the spring restoring force would harden, and in the negative direction the spring restoring force would first soften before then hardening.

4.1.2 State–Space Structural Form

The structural system equations of motion given in Eq. (27) are arranged in matrix form as

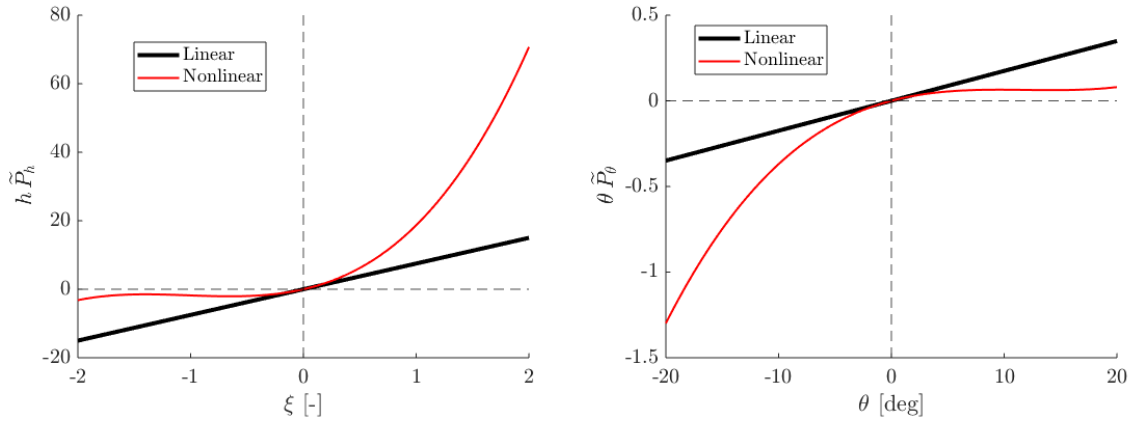

(a) Plunge (b) Pitch

Figure 3: Plunge and pitch polynomial expressions.

$$\boldsymbol{M}_{st}\ddot{\boldsymbol{x}}_d + \boldsymbol{K}_{st}\left(\boldsymbol{x}_d\right)\boldsymbol{x}_d = \boldsymbol{Q} \tag{30}$$

where

$$\boldsymbol{M}_{st} = \begin{bmatrix} m & S_\theta \\ S_\theta & I_\theta \end{bmatrix} \qquad \boldsymbol{K}_{st}\left(\boldsymbol{x}_d\right) = \begin{bmatrix} m\,\omega_h^2\,\tilde{P}_h\left(h\right) & 0 \\ 0 & I_\theta\,\omega_\theta^2\,\tilde{P}_\theta\left(\theta\right) \end{bmatrix}$$

$$\boldsymbol{x}_d = \begin{Bmatrix} h \\ \theta \end{Bmatrix} \qquad \boldsymbol{Q} = \begin{Bmatrix} -L \\ M^* \end{Bmatrix}.$$

Here, $-L$ and M^* are the lift and pitching moment. Lift is defined by convention as positive downwards.

4.2 Aerodynamic System

The formulation of the aerodynamic system follows Ref. [9], where aerodynamic indicial response function approximations are represented in state–space form. The state–space formulation of the aerodynamics provides a straightforward approach to coupling with the structural system.

The use of indicial response functions is a well–established method for representing sectional unsteady aerodynamic loads in response to arbitrary forcing via Duhamel superposition [6]. Ref. [10] first derived the indicial lift response through the Wagner function, providing an exact solution in terms of Bessel functions for incompressible flows. Large–scale, repetitive evaluation of these Bessel functions is often impractical for most use cases however, thus motivating approximations. Jones' two–pole exponential approximation [11] has seen widespread use for incompressible flows.

Ref. [12] identified the separation of unsteady aerodynamic responses in lift and pitching moment into two components; a circulatory component; and a noncirculatory component. These components relate respectively to a response generated due to shed vortices by the body, which develop over time, and, to an instantaneous response generated by the displacement of fluid by the body. For compressible flows, Ref. [13] first saw to the development of circulatory component indicial response functions for mid to high subsonic Mach numbers.

The relations used in this work for normal force and pitching moment due to step changes in angle of attack, pitch rate and vertical gust velocity are given below. These response functions follow the formulation of Ref. [9]. A modification providing generalisation for an arbitrary elastic axis location is also included from Ref. [14]. The contribution pertaining to the gust is described in Ref. [15].

$$\frac{C_{N_\alpha}(\tau)}{\alpha} = \frac{4}{M}\phi_\alpha^I(\tau,\, M) + C_{l_\alpha}\phi_\alpha^C(\tau,\, M) \tag{31}$$

$$\frac{C_{M_\alpha^*}(\tau)}{\alpha} = -\frac{1}{M}\phi_{\alpha\,M^*}^I(\tau,\, M) + C_{l_\alpha}\phi_\alpha^C(\tau,\, M)\left(\frac{1}{4} - x_{ac}(M)\right) \tag{32}$$

$$\frac{C_{N_q}(\tau)}{q} = 2(1 - x_{ea})\frac{1}{M}\phi_q^I(\tau,\, M) + \frac{3 - 4\,x_{ea}}{2}\frac{C_{l_\alpha}}{2}\phi_q^C(\tau,\, M) \tag{33}$$

$$\frac{C_{M_q^*}(\tau)}{q} = -\frac{7}{12\,M}\phi_{qM^*}^I(\tau,\, M) - \frac{C_{l_\alpha}}{16}\phi_{qM^*}^C(\tau,\, M) \tag{34}$$

$$\frac{C_{N_{w_g}}(\tau)}{w_g} = C_{l_\alpha}\phi_{w_g}^C(\tau,\, M) \tag{35}$$

In the above relations, C_{N_α} and C_{N_q} are the normal force coefficients due to step changes in angle of attack and pitch rate respectively. The terms $C_{M_\alpha^*}$ and $C_{M_q^*}$ are the pitching moment coefficients due to step changes in angle of attack and pitch rate respectively. $C_{N_{w_g}}$ is the normal force coefficient due to a step change in vertical gust velocity. x_{ac} and x_{ea} refer to the distance from the aerofoil leading edge to the aerodynamic centre, and the distance from the aerofoil leading edge to the elastic axis, respectively, both non–dimensionalised by the chord c. The terms ϕ_α^C, ϕ_α^I, $\phi_{\alpha\,M^*}^I$, ϕ_q^C, $\phi_{q\,M^*}^C$, $\phi_{q\,M^*}^I$ and $\phi_{w_g}^C$ are the indicial response functions. The superscript C and I denote a circulatory and noncirculatory component. The subscript M^* denotes an indicial function for the pitching moment response. τ is a measure of non–dimensional time, defined as $\tau = \frac{2Vt}{c}$.

4.3 State–Space Aerodynamic Form

The exponential approximations of these indicial response functions, and their equivalent state–space representations are given in Ref. [9] and Ref. [15]. For clarity, the process to obtain a component of the normal force coefficient in state–space form is shown in the following.

The normal force coefficient has four components; a circulatory normal force component; an instantaneous normal force component due to step changes in angle of attack; an instantaneous normal force component due to step changes in pitch rate; and, a normal force component due to gust disturbance. The following focuses on the circulatory normal force component.

The indicial circulatory response due to step changes in angle of attack is approximated by the two–pole exponential function

$$\phi_\alpha^C(\tau,\, M) = 1 - A_1\text{exp}\left(-b_1\beta^2\,\tau\right) - A_2\text{exp}\left(-b_2\beta^2\,\tau\right) \tag{36}$$

where, $\beta = \sqrt{1 - M^2}$, which is the Prandtl–Glauert factor for compressibility. The constants of the exponential function are given as $A_1 = 0.30$, $A_2 = 0.70$, $b_1 = 0.14$ and $b_2 = 0.53$.

From this exponential approximation, the circulatory normal force response to a step change in angle of attack can be written in state–space form as

$$\begin{bmatrix} \dot{x}_1 \\ \dot{x}_2 \end{bmatrix} = \left(\frac{2\,V}{c} \right) \beta^2 \begin{bmatrix} -b_1 & 0 \\ 0 & -b_2 \end{bmatrix} \begin{bmatrix} x_1 \\ x_2 \end{bmatrix} + \begin{bmatrix} 1 \\ 1 \end{bmatrix} \alpha_{3/4}\,(t) \tag{37}$$

where $\alpha_{3/4}$ is the angle of attack at the three–quarters–chord, given by

$$\alpha_{3/4}\,(t) = \alpha\,(t) + \frac{(3 - 4\,x_{ea})\,q\,(t)}{2}. \tag{38}$$

This permits expression of the state–space system as

$$\begin{bmatrix} \dot{x}_1 \\ \dot{x}_2 \end{bmatrix} = \left(\frac{2\,V}{c} \right) \beta^2 \begin{bmatrix} -b_1 & 0 \\ 0 & -b_2 \end{bmatrix} \begin{bmatrix} x_1 \\ x_2 \end{bmatrix} + \begin{bmatrix} 1 & \frac{3-4\,x_{ea}}{2} \\ 1 & \frac{3-4\,x_{ea}}{2} \end{bmatrix} \begin{Bmatrix} \alpha\,(t) \\ q\,(t) \end{Bmatrix} \tag{39}$$

or more conveniently as

$$\begin{bmatrix} \dot{x}_1 \\ \dot{x}_2 \end{bmatrix} = \begin{bmatrix} a_{11} & 0 \\ 0 & a_{22} \end{bmatrix} \begin{bmatrix} x_1 \\ x_2 \end{bmatrix} + \begin{bmatrix} b_{11} & b_{12} \\ b_{21} & b_{22} \end{bmatrix} \begin{Bmatrix} \alpha\,(t) \\ q\,(t) \end{Bmatrix}. \tag{40}$$

The output equation for the circulatory normal force coefficient is given by

$$C_N^C\,(t) = C_{N_\alpha} \frac{2\,V}{c} \beta^2 \begin{bmatrix} A_1 b_1 & A_2 b_2 \end{bmatrix} \begin{bmatrix} x_1 \\ x_2 \end{bmatrix} \tag{41}$$

which is written in the form

$$C_N^C\,(t) = \begin{bmatrix} c_{11} & c_{12} \end{bmatrix} \begin{bmatrix} x_1 \\ x_2 \end{bmatrix}. \tag{42}$$

This system of 2 ODEs describes the combined circulatory normal force component due to step changes in angle of attack and pitch rate. The remaining unsteady aerodynamic contributions, including the gust, are represented with a further 8 ODEs. The total unsteady aerodynamic response in normal force and pitching moment can then be described by a combined system of 10 ODEs, which is given below as

$$\dot{\boldsymbol{x}}_{\boldsymbol{a}} = \boldsymbol{A}\,\boldsymbol{x}_a + \boldsymbol{B}\,\boldsymbol{u}_a + \boldsymbol{B}_g\,u_g \tag{43}$$

with output equation

$$\begin{Bmatrix} C_N \\ C_{M^*} \end{Bmatrix} = \boldsymbol{C}\boldsymbol{x}_a + \boldsymbol{D}\,\boldsymbol{u}_a \tag{44}$$

where the aerodynamic input and gust disturbance vectors have been redefined as given below to simplify notation:

$$\boldsymbol{u}_a = \begin{Bmatrix} \alpha \\ q \end{Bmatrix} \qquad \boldsymbol{u}_g = \left\{ \tfrac{w_g}{V_\infty} \right\}. \tag{45}$$

In the 10 ODE system of Eq. 43, 8 ODEs describe the unsteady aerodynamic response of the aerofoil to changes in angle of attack and pitch rate, and 2 ODEs describe the unsteady aerodynamic response of the aerofoil to gust disturbance. The reader is directed to Ref [9] and Ref [16] for detail on the aerofoil aerodynamic contributions to $\boldsymbol{A}$, $\boldsymbol{B}$, $\boldsymbol{C}$ and $\boldsymbol{D}$. The gust contributions in the disturbance matrix $\boldsymbol{B}_g$ and in the matrices $\boldsymbol{A}$ and $\boldsymbol{C}$ are given in Ref [15].

4.4 State–Space Aeroelastic Form

The state–space system describing the total unsteady aerodynamic response may now be coupled with the structural equations to form an aeroelastic system. This coupling is as described in Ref. [17] and Ref. [18]. For completeness these steps are repeated in the following.

The vector of aerodynamic forces can be expressed as

$$\begin{Bmatrix} -L \\ M^* \end{Bmatrix} = \frac{1}{2}\rho V_\infty \begin{bmatrix} -c & 0 \\ 0 & c^2 \end{bmatrix} \begin{Bmatrix} C_N \\ C_{M^*} \end{Bmatrix} = \boldsymbol{T}_2 \begin{Bmatrix} C_N \\ C_{M^*} \end{Bmatrix}, \tag{46}$$

and now recalling the total unsteady aerodynamic output equation of Eq. (44), can be written as

$$\begin{Bmatrix} -L \\ M^* \end{Bmatrix} = \boldsymbol{T}_2 \left(\boldsymbol{C}\boldsymbol{x} + \boldsymbol{D}\,\boldsymbol{u}_a \right). \tag{47}$$

The state–space aerodynamic input quantities, α and q are now expressed in terms of the structural system displacements h and θ such that

$$\boldsymbol{u}_a = \begin{bmatrix} 0 & 1 \\ 0 & 0 \end{bmatrix} \begin{Bmatrix} h \\ \theta \end{Bmatrix} + \begin{bmatrix} 1/U & 0 \\ 0 & c/U \end{bmatrix} \begin{Bmatrix} \dot{h} \\ \dot{\theta} \end{Bmatrix} = \boldsymbol{T}_{11}\boldsymbol{x}_d + \boldsymbol{T}_{12}\boldsymbol{x}_v. \tag{48}$$

The aerodynamic force vector may then be written as

$$\boldsymbol{Q} = \boldsymbol{T}_2 \left(\boldsymbol{C}\boldsymbol{x}_a + \boldsymbol{D}\boldsymbol{T}_{11}\boldsymbol{x}_d + \boldsymbol{D}\boldsymbol{T}_{12}\boldsymbol{x_v} \right). \tag{49}$$

Similarly, the state–space aerodynamic input equations may be written as

$$\dot{\boldsymbol{x}}_a = \boldsymbol{A}\boldsymbol{x}_a + \boldsymbol{B}\boldsymbol{T}_{11}\boldsymbol{x}_d + \boldsymbol{B}\boldsymbol{T}_{12}\boldsymbol{x}_v + \boldsymbol{B}_g\, u_g. \tag{50}$$

The state–space aeroelastic system can then be written as

$$\begin{bmatrix} \boldsymbol{I} & \boldsymbol{0} & \boldsymbol{0} \\ \boldsymbol{0} & \boldsymbol{M}_{st} & \boldsymbol{0} \\ \boldsymbol{0} & \boldsymbol{0} & \boldsymbol{I} \end{bmatrix} \begin{Bmatrix} \dot{\boldsymbol{x}}_d \\ \dot{\boldsymbol{x}}_v \\ \dot{\boldsymbol{x}}_a \end{Bmatrix} = \begin{bmatrix} \boldsymbol{0} & \boldsymbol{I} & \boldsymbol{0} \\ \boldsymbol{T}_2\boldsymbol{D}\boldsymbol{T}_{11} - \boldsymbol{K}_{st}\left(\boldsymbol{x}_d\right) & \boldsymbol{T}_2\boldsymbol{D}\boldsymbol{T}_{12} & \boldsymbol{T}_2\boldsymbol{C} \\ \boldsymbol{B}\boldsymbol{T}_{11} & \boldsymbol{B}\boldsymbol{T}_{12} & \boldsymbol{A} \end{bmatrix} \begin{Bmatrix} \boldsymbol{x}_d \\ \boldsymbol{x}_v \\ \boldsymbol{x}_a \end{Bmatrix} + \begin{bmatrix} \boldsymbol{0} \\ \boldsymbol{0} \\ \boldsymbol{B}_g \end{bmatrix} u_g \tag{51}$$

where $\boldsymbol{I}$ is an identity matrix. The aeroelastic mass matrix, $\boldsymbol{M}_{ae}$ is on the left hand side of the system of equations. Pre–multiplying both sides by $\boldsymbol{M}_{ae}^{-1}$ then leads to the system of equations

$$\dot{\boldsymbol{X}} = \boldsymbol{A}_{ae}\left(\boldsymbol{x}_d\right)\boldsymbol{X} + \boldsymbol{B}_{g,ae}\, u_g \tag{52}$$

where $\boldsymbol{A}_{ae}$ is the aeroelastic system matrix, which is a function of the structural displacements $\boldsymbol{x}_d$. $\boldsymbol{B}_{g,ae}$ is the aeroelastic gust disturbance matrix.

Eq. 52 describes the FOM used in this work. The FOM has state–space dimension 14. The external disturbance vector, u_g, has 1 element relating to gust disturbance.

Table 2: Full Order Model Parameters

M	$= 0.850$
μ	$= 100.000$
r_θ	$= 0.500$
c	$= 15.000\, ft$
ω_h	$= 10.000\, rad\, s^{-1}$
ω_θ	$= 50.000\, rad\, s^{-1}$
$C_{l\alpha}$	$= 14.650\, rad^{-1}$
x_{ac}	$= 0.286$
x_θ	$= 0.250$
x_{ea}	$= 0.250$

5 FULL ORDER MODEL ANALYSES

In this section analyses of the FOM are performed. First, a linear system stability analysis is performed, which is a prerequisite to MOR by the method described in Section 3. An analysis of the FOM dynamics is then presented. The analyses of the dynamics is used to observe the differences between the linear and nonlinear dynamical systems, and, to determine disturbances causing the worst–case dynamic response.

The aerofoil structural parameters and flight conditions used in this work are given in Table 2. Parameters and conditions may be assumed as those given in Table 2 unless specified otherwise.

Values for the speed of sound a and density ρ have been defined according to the ISA at an altitude of $32,808\, ft$. Aerofoil mass per spanwise unit length, static mass moment and mass moment of inertia are computed via the respective relations $m = \mu\, \pi\, \rho\, b^2$, $S_\theta = m\, b\, x_\theta$ and $I_\theta = m\, b^2\, r_\theta^2$, where μ is mass ratio and r_θ is radius of gyration about the elastic axis. In this work, aerofoil mass is computed using a separate value of density according to the ISA at an altitude of $15,000\, ft$.

5.1 Linear System Stability Analysis

Towards creating ROMs of the dynamical system according to the method described in Section 3, a linear system stability analysis is required. Performing this analysis collects the necessary information of the eigenspectrum, and permits some meaning to be assigned to this information.

The aeroelastic system is defined in equilibrium over a density range. This density range is from the density given by the ISA at $32,808\, ft$, to a density of zero. The aeroelastic state vector at equilibrium for each density increment is $\mathbf{0}$. Evaluating the aeroelastic system matrix $\boldsymbol{A}_{ae}$ at equilibrium yields the Jacobian matrix. Eigenvalue problems of the Jacobian matrix are computed at each density increment. At zero density, the fluid and structural systems are decoupled.It is then possible to identify the eigenvalues (and associated eigenvectors) corresponding to bending and torsion in the structural system, and, to the indicial response functions in the aerodynamic system by following the eigenvalue traces from the decoupled system, into, and through the coupled system.

5.1.1 Aeroelastic Mode Tracking

Before proceeding with the root–locus for varying density, complications are noted to arise when solving these types of sequential eigenvalue problems. One difficulty is that there is no

guarantee the eigenvalues resultant from commercially available eigenvalue solvers will be ordered in a physically consistent way. This necessitates a sorting algorithm. The simplest means of sorting the eigenbasis is by eigenvalue frequency content. However, this sorting mechanism may be problematic where mode crossing occurs. Mode crossing is where as the parameter of interest, for example density is varied, the eigenvalue traces corresponding to certain modes may cross multiple times.

A mechanism to sort the eigenbasis over a varying parameter range is presented in Ref [19], which uses the bi–orthogonality of the left and right eigenvectors. Sorting by this method is convenient as the left and right eigenvalue problems are required in the construction of the ROMs considered in this work. Thus, with little extra computational effort on top of what is already required to construct ROMs over the varying parameter range, it is possible to sort the eigenbasis to ensure physical consistency between parameter increments.

The method of Ref [19] is detailed in the following. For two consecutive parameter increments with Jacobian matrices $\boldsymbol{A}_i$ and $\boldsymbol{A}_{i+1}$, the bi–orthogonality conditions of the left and right eigenvectors will be satisfied such that

$$\bar{\boldsymbol{\Psi}}_i^T \boldsymbol{\Phi}_i \;=\; \boldsymbol{I} \tag{53}$$

$$\bar{\boldsymbol{\Psi}}_{i+1}^T \boldsymbol{\Phi}_{i+1} \;=\; \boldsymbol{I} \tag{54}$$

A matrix is computed by projection of the set of left eigenvectors of the current parameter increment onto the set of right eigenvectors of the next parameter increment as

$$\boldsymbol{S}_{i,\,i+1} \;=\; \bar{\boldsymbol{\Psi}}_i^T \boldsymbol{\Phi}_{i+1}. \tag{55}$$

Providing that the parameter increment is sufficiently small, bi–orthogonality will be approximately satisfied between the left and right eigenvectors of different parameter increments. Thus, the matrix $\boldsymbol{S}_{i,\,i+1}$ on being appropriately sorted will be diagonally dominant. Applying the diagonally sorted order of the matrix $\boldsymbol{S}_{i,\,i+1}$ to the eigenbasis at the next parameter increment will enforce that $\boldsymbol{\Psi}_{i+1}$ and $\boldsymbol{\Phi}_{i+1}$ are sorted according to $\boldsymbol{\Psi}_i$.

An example of the matrix $\boldsymbol{S}_{i,\,i+1}$ prior to, and after sorting is shown in Figure 4 in terms of absolute value. In the left panel, the matrix is unsorted, in the right panel the matrix is sorted. The indices of this sorted matrix are applied to the eigenbasis at the $i+1^{th}$ parameter increment. Bar height is different along the diagonal as the left and right eigenvectors are scaled according to Eq. (10) when purely real, and according to Eq. (7) when complex valued.

It is noted that the above sorting mechanism requires solutions of the left and right eigenvalue problems at each parameter increment. Ref. [19] provides a method which only requires solution of the left eigenvalue problem every other parameter increment. As this work makes use of the left and right eigenvalue problems in ROM construction, both eigenvalue problems are solved at each parameter increment. The sorting mechanism used here reflects this, thus the left and right eigenvectors are used at each increment in the sorting algorithm.

5.1.2 Mode Identification

As mentioned previously, it is possible to identify the physical and mathematical phenomena that the eigenvalues and associated eigenvectors correspond to.

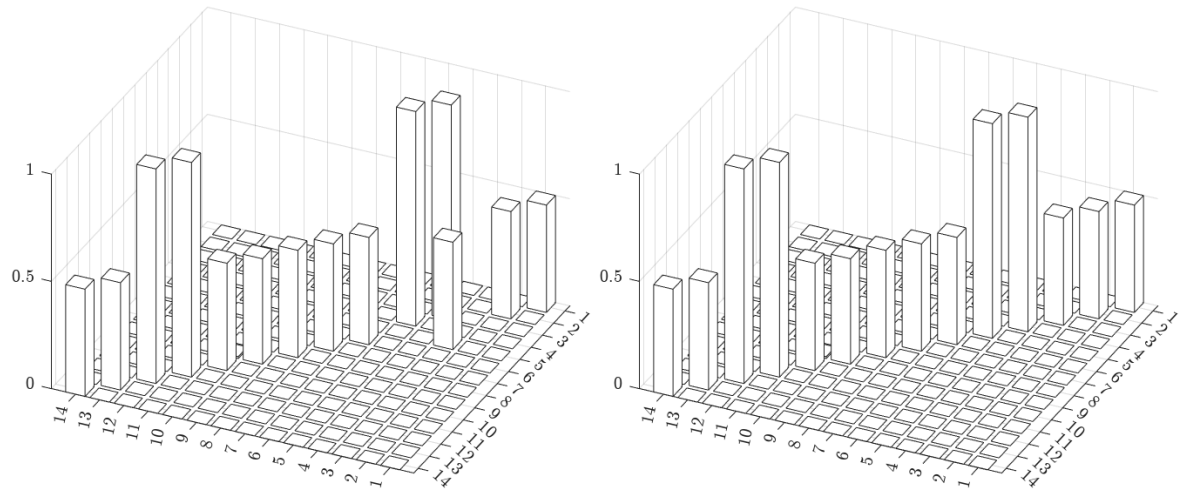

(a) Unsorted $\boldsymbol{S}_{i,\,i+1}$ (b) Sorted $\boldsymbol{S}_{i,\,i+1}$

Figure 4: Example of the sorting algorithm on $\boldsymbol{S}_{i,\,i+1}$

Identification of the structural modes is performed by following the eigenvalue traces over a density range tending to zero. At zero–density, the pure structural system frequencies are identified. This is shown in the root–locus of Figure 5, which has been truncated near the origin to emphasise the structural eigenvalues. The maximum and minimum densities are marked in the Figure. It is seen in Figure 5 that as density decreases, the complex eigenvalues tend towards the imaginary axis. At zero–density, these eigenvalues have no real component, and are identical to the eigenvalues of the pure structural system. The bending and torsional modes have been labelled in Figure 5.

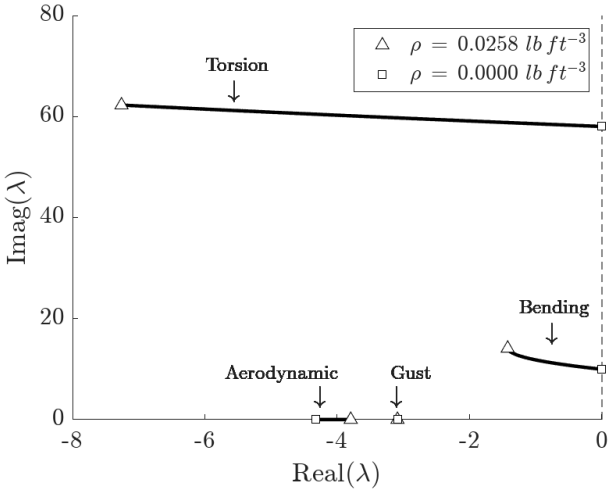

Figure 5: Eigenvalue variation with density tending to zero.

The modes pertaining to the gust dynamics are separately identifiable. The indicial response function approximation for the gust dynamics is given in Ref. [15] as a two–pole exponential function of a form similar to Eq. (36). Within each of the exponential function terms there is a constant value. These constants are $\epsilon_1\,\beta^2$ and $\epsilon_2\,\beta^2$, which correspond to the slow and fast dynamics of the gust contribution. The modes pertaining to the slow and fast gust dynamics are identifiable by non–dimensionalisation of the eigenvalues (in radians) by the constant terms $\epsilon_1\,\beta^2$ and $\epsilon_2\,\beta^2$. These modes are always identifiable and do not require decoupling of the fluid

and structural systems by tending density to zero. The lowest frequency gust mode is marked in Figure 5. It is seen that as density tends to zero, the real part of the gust mode does not vary. This is due to the gust contribution being independent of the structural states.

The remaining modes correspond to the indicial response functions ϕ^C_α, ϕ^I_α, $\phi^I_{\alpha\,M^*}$, ϕ^C_q, $\phi^C_{q\,M^*}$ and $\phi^I_{q\,M^*}$. These modes are identified by non–dimensionalising the eigenvalues (in radians) of the decoupled fluid system by the constant terms in the exponentials of the remaining indicial response functions. The eigenvalue traces can be followed in the same way as for the structural system mode identification. For example, the indicial circulatory response function due to step changes in angle of attack given by Eq. (36), has two poles. Non–dimensionalising the eigenvalues (in radians) at zero density by the terms in each exponential; $b_1\beta^2$ and $b_2\beta^2$, will reveal the eigenvalues corresponding to the low frequency and high frequency indicial circulatory lift due to angle of attack component. The low frequency component of indicial circulatory lift due to angle of attack is labelled in Figure 5 as "Aerodynamic.". It is seen that as density tends to zero, the real part of this eigenvalue varies, which is due to the coupling of α and q in the structural states h and θ.

The modal basis at $32,808\,ft$ is given in Table 3. The basis is sorted in order of increasing frequency content. The decoupled system each mode originates from is stated in Table 3 as either "Gust", "Aerodynamic" or "Structural".

Table 3: Full Order Model eigenvalues at $32,808\,ft$

Index	Origin	Mode	Eigenvalue	Frequency $[Hz]$
1	Gust	$\phi^C_{w_g}$	$-3.0901 + 0.0000\,i$	0.4918
2	Aerodynamic	ϕ^C_α	$-3.7962 + 0.0000\,i$	0.6042
3	Aerodynamic	$\phi^C_{q\,M^*}$	$-9.6115 + 0.0000\,i$	1.5297
4	Structural	Bending	$-1.4249 + 14.0906\,i$	2.2540
5	Aerodynamic	ϕ^C_α	$-14.8248 + 0.0000\,i$	2.3594
6	Aerodynamic	Torsion*	$-36.7824 + 1.9264\,i$	5.8621
7	Gust	$\phi^C_{w_g}$	$-42.2414 + 0.0000\,i$	6.7229
8	Aerodynamic	ϕ^I_α	$-43.6129 + 0.0000\,i$	6.9412
9	Structural	Torsion	$-7.2598 + 62.2707\,i$	9.9777
10	Aerodynamic	ϕ^I_q	$-73.9035 + 0.0000\,i$	11.7621
11	Aerodynamic	$\phi^I_{\alpha\,M^*}$	$-102.6123 + 0.0000\,i$	16.3313

Table 3 contains a mode labelled "Torsion*". At $32,808\,ft$ this mode strongly relates to torsion. However, at zero density, it originates in the decoupled aerodynamic system. As density is decreased to zero and the aerodynamic system decouples, this complex conjugate pair of eigenvalues becomes two distinct purely real eigenvalues, which correspond to the slow dynamics of $\phi^I_{\alpha\,M^*}$ and to $\phi^I_{q\,M^*}$, which are the instantaneous component indicial response functions for pitching moment in angle of attack and pitch rate respectively. In Ref [17], it is stated that this complex eigenvalue corresponds to a torsional mode coupled with the unsteady aerodynamics.

5.2 Flutter Search

A flutter search of the linear system is also performed by analysis of the eigenspectrum over varying Mach number. The flutter search is executed at a fixed altitude of $9,843\,ft$ with local speed of sound and air density according to the ISA at this altitude. Mach number is varied in small increments from $M = 0.01$ to $M = 0.90$. The flutter search is performed with the lift curve slope given in Table 2. In reality, as Mach number varies, the lift curve slope and

aerodynamic centre location will also vary. The lift curve slope and aerodynamic centre location given in Table 2 are valid only at $M = 0.85$. These values were based on the results of transonic small disturbance codes discussed briefly in Ref. [17]. The Prandtl–Glauert correction may be used to account for the variation of lift curve slope with Mach number. Experimental methods or CFD analyses as discussed in Ref. [17] are required for the variation of aerodynamic centre location with Mach number. For simplicity, this work keeps Mach number and the aerodynamic centre fixed at the value appropriate for $M = 0.85$ according to Ref. [17].

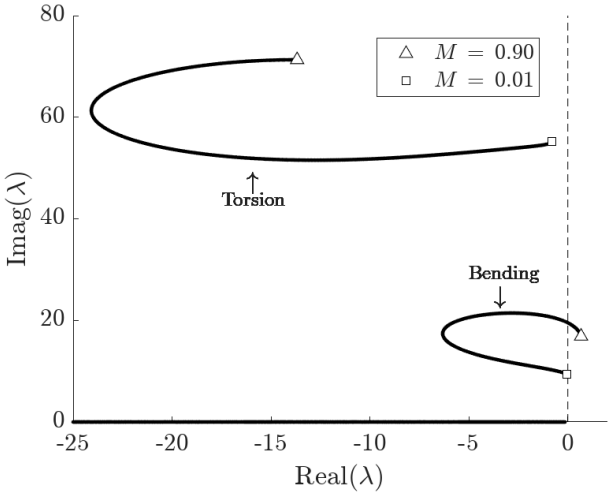

Figure 6: Eigenvalues over Mach range.

It is seen in Figure 6 that the mode originating as bending in the decoupled structural system becomes the flutter mode, and crosses the imaginary axis at approximately $M = 0.833$. The dynamics of the linear system at Mach numbers greater than $M = 0.833$ will diverge. The dynamics of the structurally nonlinear system are however not so predictable. Depending on the type of structural nonlinearity, the dynamic response may settle into small amplitude stable limit cycle oscillations, or may diverge more rapidly. An analysis of these nonlinear dynamics is performed in a subsequent section.

5.3 Full Order Model Dynamic Response

The dynamic response of the FOM is considered for three cases. The first case is for a perturbation in the initial conditions, without gust–excitation. The second case is for the system being excited from equilibrium by gust disturbance. The third case considers the post–flutter dynamic response. The nonlinear model, denoted by NFOM uses the nonlinear structural parameters given in Table 1. The linear model, denoted by LFOM, sets the parameters pertaining to the quadratic and cubic nonlinearities to zero, thus resulting in a linear structural model.

5.3.1 Initial Condition

The system is perturbed from equilibrium with a non–zero pitch displacement in the initial conditions. A small perturbation in pitch of 0.1 degrees is considered first. It is seen in Figure 7 that for this small perturbation the dynamics in pitch for the linear and nonlinear systems are nearly identical. Differences are observable in the plunge dynamics, however these differences are small. The dynamics of the linear and nonlinear systems being very similar is due to the initial perturbation being small enough that structural nonlinearities in the spring restoring force are not dominant over the linear spring restoring force.

A larger perturbation of 15.0 degrees is now considered. This perturbation is chosen as it is

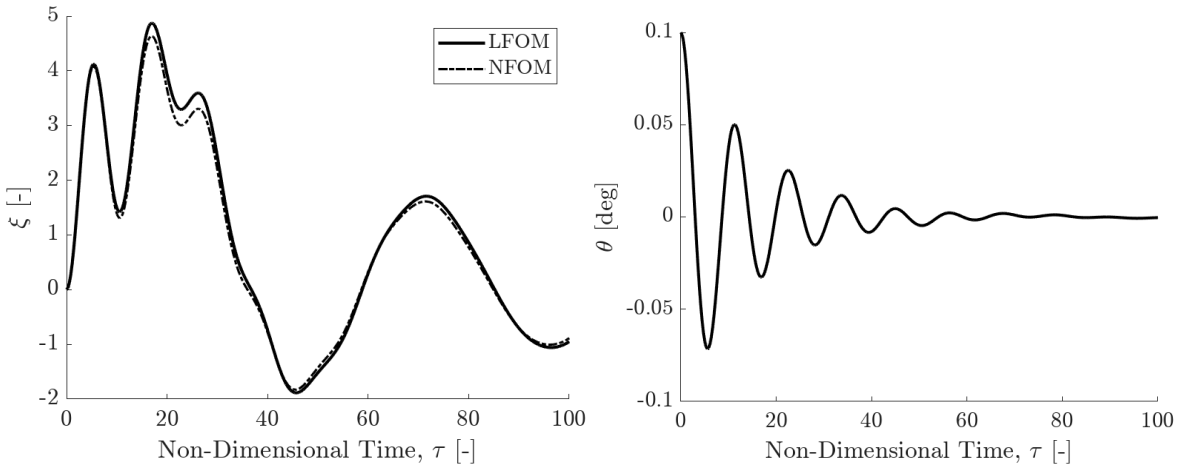

(a) Non–dimensional plunge (b) Pitch

Figure 7: Linear and nonlinear FOM dynamics for a 0.1 degree pitch initial condition.

sufficiently large to ensure the dynamics of the structure are nonlinear, while still being within the region of validity of the linear indicial aerodynamic model used (< 20.0 degrees). Results for the 15.0 degree perturbation are shown in Figure 8. The differences between the linear and nonlinear dynamics are more apparent. With respect to the pitch degree of freedom, it is noticeable that the nonlinear dynamics are more restrained than the linear dynamics in negative pitch displacement. This is consistent with the pitch nonlinearity shown in Figure 3, which has a spring hardening effect in negative pitch displacement. With respect to the plunge degree of freedom, it is seen that initially the nonlinear model displaces negatively, while the linear model displaces positively. This behaviour follows the plunge nonlinearity shown in Figure 3, which for negative plunge displacement, the restoring force of the spring plateaus in comparison to the linear spring restoring force.

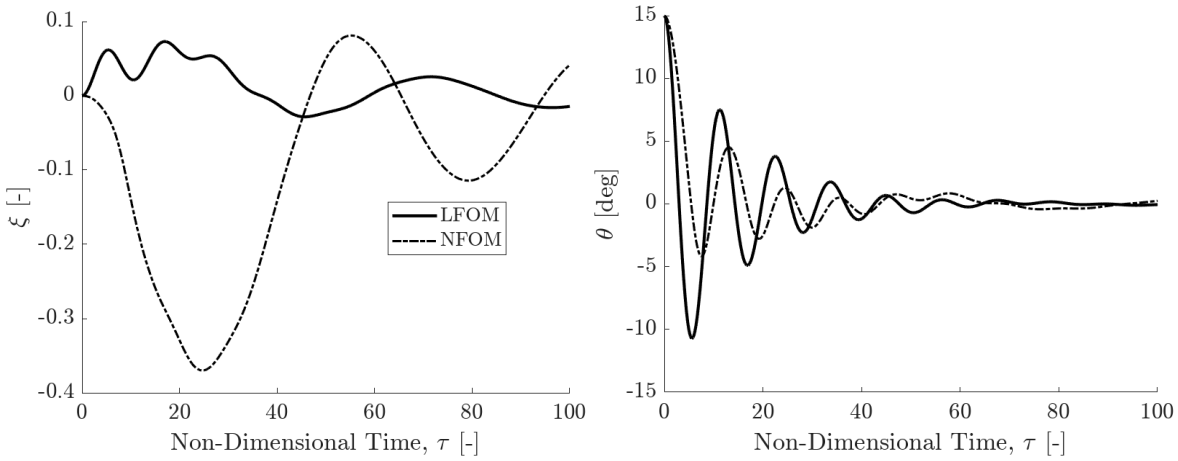

(a) Non–dimensional plunge (b) Pitch

Figure 8: Linear and nonlinear FOM dynamics for a 15.0 degree pitch initial condition.

5.3.2 Gust Excitation

An analysis of the dynamic response due to gust disturbance is performed in this section. This work considers the discrete one–minus cosine shaped gust of the form

$$w_g(\tau) = \frac{1}{2} W_0 \left(1 - \cos\left(2\pi\, h_g^{-1}(\tau - \tau_0)\right)\right) \qquad \text{for} \quad \tau_0 \leq \tau \leq \tau_0 + h_g n_c, \tag{56}$$

where W_0 is the gust peak intensity, h_g is the gust wavelength, n_c is the number of cycles and τ_0 is the time at which the gust input is applied. The discrete one–minus–cosine gust is defined according to the FAA AC 25.341–1 [20]. These discrete gust forms are used to represent single extreme turbulence events, such as those at the edges of thermals and downdrafts, in the wakes of structures or mountains, or at temperature inversions [4]. Such extremes are not considered in standard continuous random turbulence models. In the interest of studying the dynamic response for a worst-case gust search, or for control design for gust-load alleviation, it is appropriate then to use the one-minus-cosine gust profile.

The gust intensity is defined according to the FAA AC 25.341–1 [20], using parameters that are dependent on the aircraft and its configuration, flight conditions, and the gust gradient. As this work considers a test–case not specific to a whole aircraft, those relevant parameters have been set to a value to maximise the gust intensity. The gust gradient is the distance over which the gust velocity increases to a maximum value. The gust gradient is specified as ranging from $30\ ft$ to $350\ ft$ in the FAA AC–25.34–1 [20]. The range of gust profiles used is given in Figure 9.

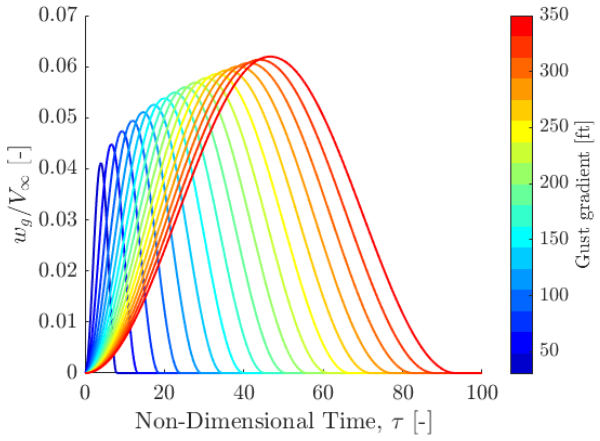

Figure 9: One–minus cosine gust profiles.

In the following, a study is performed to assess the dynamic response of the linear and nonlinear systems to the range of gust profiles given in Figure 9. Such an analysis is typically performed to determine the worst case dynamic response of the system to gust excitation. In this case the objective is to compare the linear and nonlinear dynamics, and, to determine the gust excitation causing ”interesting” dynamics. A specific gust excitation will be chosen based on the search performed here for the ROM generation study in the subsequent section.

The dynamics of the linear and nonlinear systems in response to excitation by the range of gust profiles is given in Figure 10. In the left column the linear dynamics are shown. In the right column, the nonlinear dynamics are shown. The colours of the curves in Figure 10 align with the gust gradient colour bar in Figure 9.

With respect to non–dimensional plunge, it is seen that the peak displacement in the linear and nonlinear dynamical systems both occur at the maximum gust gradient of $350\ ft$. There is a

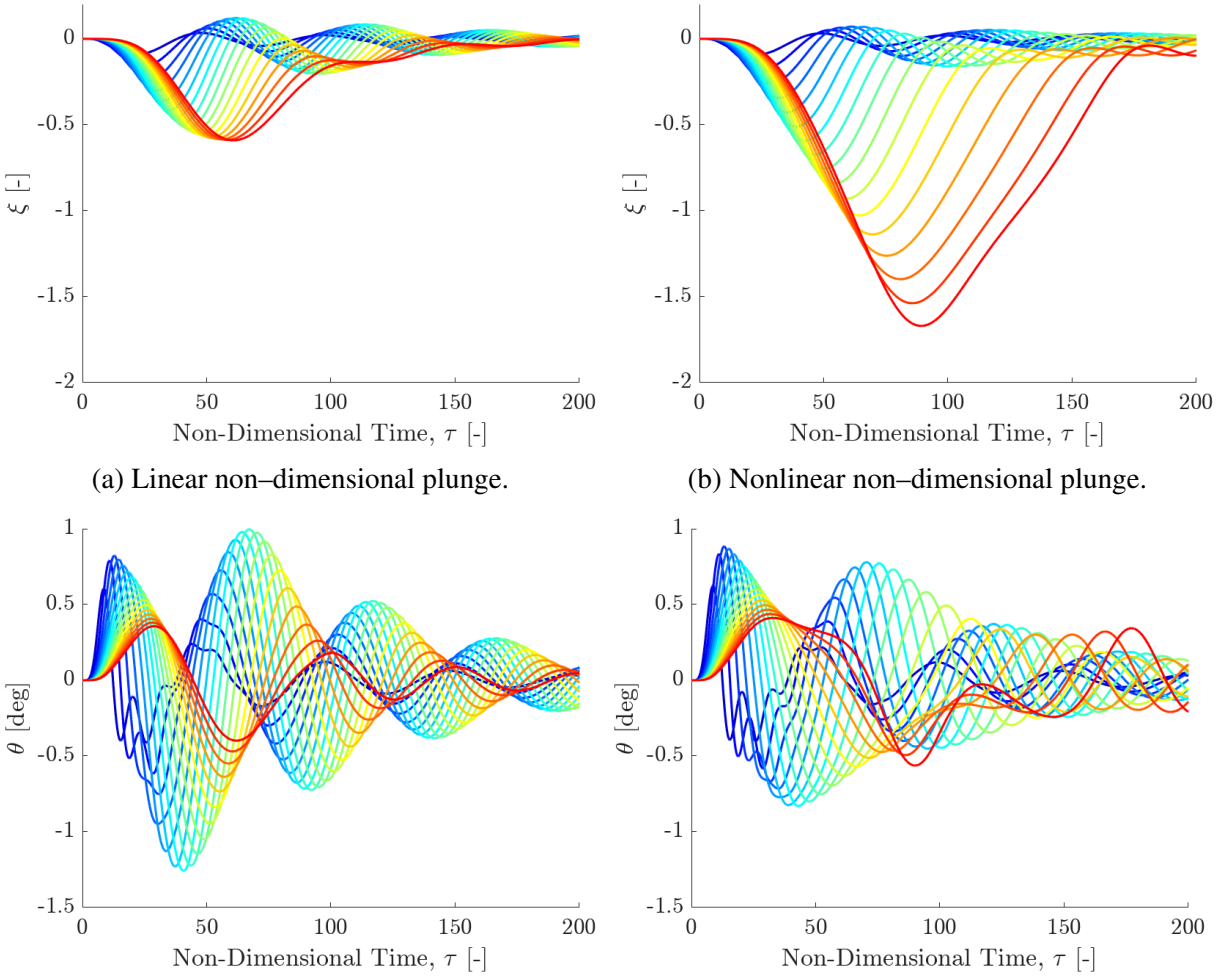

(a) Linear non–dimensional plunge.

(b) Nonlinear non–dimensional plunge.

(c) Linear pitch.

(d) Nonlinear pitch.

Figure 10: Linear system (left column) and nonlinear system (right column) dynamic responses to gusts of varying gradient.

clear difference between the linear and nonlinear dynamics in plunge, with the peak negative displacement for the nonlinear dynamics being nearly three times larger than the linear system. With respect to pitch, the peak positive and negative displacement of both the linear and nonlinear systems do not occur at the maximum gust gradient. For the linear dynamical system, the peak positive and negative pitch displacements are at gust gradients of $170\ ft$ and $150\ ft$ respectively. For the nonlinear dynamical system, the peak positive pitch displacement occurs at $60\ ft$ and the peak negative pitch displacement occurs at $150\ ft$.

The peak positive and negative displacements in plunge and pitch are plotted across the gust gradient range in Figure 11. The difference between the linear and nonlinear dynamics in terms of maximum displacement is more clear here. It is seen in Figure 11 that in terms of plunge displacement, the nonlinear system exhibits the most extreme dynamics, while in terms of pitch displacement the nonlinear system is more restrained compared to the linear system.

It is clear that at the larger gust gradients, the plunge dynamics become dominated by the gust. Further increasing the gust gradient would see the dynamics tend towards the shape of the gust excitation. These dynamics would otherwise be ”uninteresting”, however, observing the curve corresponding to the $350\ ft$ gust gradient in the nonlinear pitch dynamics in Figure 10 reveals

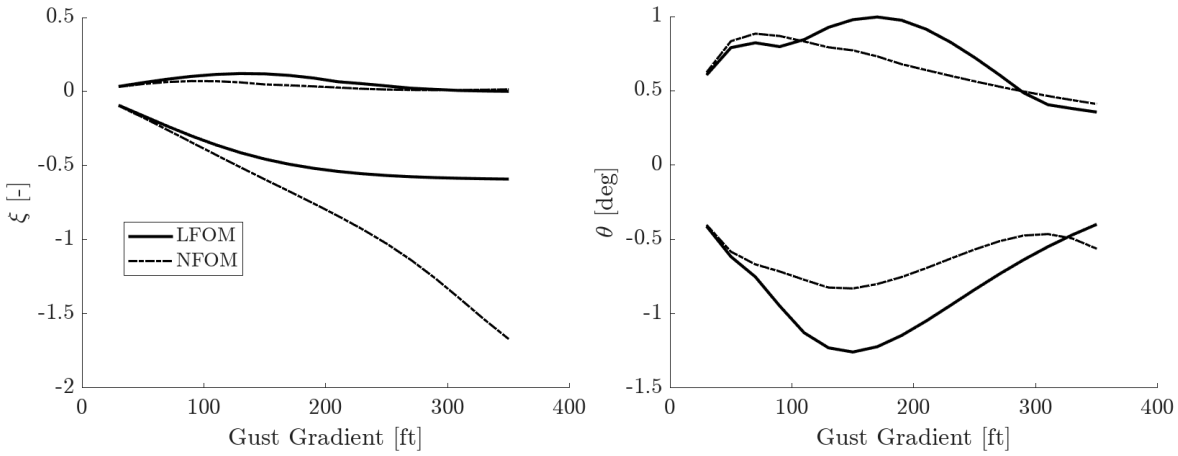

(a) Non–dimensional plunge

(b) Pitch

Figure 11: Maximum and minimum displacements of the linear and nonlinear dynamical systems over increasing gust gradient.

the dynamic response to be highly nonlinear. Thus, the gust gradient of $350\,ft$ is used as the benchmark excitation for future nonlinear ROM generation. The $150\,ft$ gust gradient is used as the benchmark excitation for linear ROM generation. These gust excitations are physical and not beyond what may be encountered in the given flight conditions. It is important for later comparison with the ROM dynamics that the excitation used is both physical and results in sufficiently interesting dynamics. Using a non–physical excitation may result in the ROM never being able to perform adequately, while an excitation that is too small may overstate the capability of the ROM.

5.4 Post–Flutter Dynamics

The dynamics of the linear and nonlinear systems are compared here in the post–flutter regime. In Section 5.2, the linear flutter boundary of the dynamical system with altitude fixed at $9,843\,ft$ was found to occur at $M = 0.833$. This analysis will use $M = 0.850$, which is past the linear flutter boundary. The dynamic response to a 15–degree pitch displacement in the initial conditions is shown in Figure 12.

It is seen in Figure 12 that the linear dynamics diverge over time, which is the expected behaviour. The nonlinear dynamics settle into stable, small amplitude limit cycle oscillations. The amplitude of these limit cycle oscillations is initially larger than the amplitude of the oscillations in the linear dynamic model.

6 REDUCED ORDER MODEL DYNAMIC RESPONSE

In this section, linear and nonlinear ROMs are created according to the methodology described in Section 3. The dynamic response of the ROMs to perturbations in the initial conditions, and, gust disturbance is compared against the equivalent linear FOM and nonlinear FOM. The analyses consider ROMs constructed using varying combinations of the modeshapes in Table 3. This results in linear and nonlinear ROMs of varying size and computational complexity. For a FOM of higher dimension, it would be beneficial to provide comparison between the computational cost of the FOM and constructed ROMs. As the dimension of the FOM system is already small and that it is computationally inexpensive to evaluate, no comparison of computational

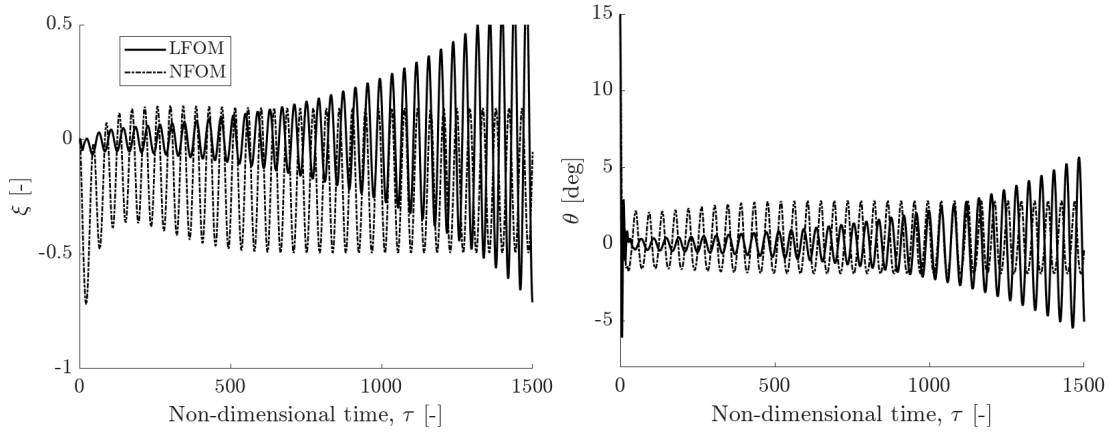

(a) Non–dimensional plunge (b) Pitch

Figure 12: Post–flutter linear and nonlinear FOM dynamics in response to a 15 degree perturbation in pitch displacement in the initial conditions.

performance is made. This study demonstrates only ROM construction, capability to capture the physics of the FOM and, the form and structure of the constructed ROMs.

6.1 Linear Aeroelastic Reduced Order Modelling

Analysis begins with the model reduction of the linear aeroelastic system. The modal bases of these linear ROMs are given in Table 4. These linear ROMs are referred to as LROMs from hereon. The dynamics of LROM_2 are studied first. LROM_2 contains only the two modes pertaining to the decoupled structural system in bending and torsion. As it is desired to observe the dynamics in plunge and pitch, the selection of the bending and torsional modes is a sensible and physical first guess.

Table 4: Modal Bases for Reduced Order Models

Index	Mode	Frequency $[Hz]$	ROM_2	ROM_3	ROM_4	ROM_6	ROM_7
1	$\phi^C_{w_g}$	0.4918		✓	✓	✓	✓
2	ϕ^C_{α}	0.6042				✓	✓
3	$\phi^C_{q\,M^*}$	1.5297				✓	✓
4	Bending	2.2540	✓	✓	✓	✓	✓
5	ϕ^C_{α}	2.3594					
6	Torsion*	5.8621			✓	✓	✓
7	$\phi^C_{w_g}$	6.7229					
8	ϕ^I_{α}	6.9412					✓
9	Torsion	9.9777	✓	✓	✓	✓	✓
10	ϕ^I_{q}	11.7621					
11	$\phi^I_{\alpha\,M^*}$	16.3313					

The dynamics of the linear FOM and LROM_2 due to a perturbation in the initial conditions is shown in Figure 13. A non–dimensional plunge displacement of 1 semi–chord and a pitch–displacement of 15–degrees is used as the initial condition. It is seen in Figure 13 that LROM_2 is able to adequately capture the shape of the free–response of the linear FOM. The dynamic response in pitch displacement is approximated very well by LROM_2. There is however a

noticeable difference in the approximation of the initial condition in non–dimensional plunge displacement. This exists due to the approximation $\boldsymbol{x}_0 \approx \boldsymbol{\Phi}\boldsymbol{z}_0 + \bar{\boldsymbol{\Phi}}\bar{\boldsymbol{z}}_0$, where $\boldsymbol{z}_0 = \bar{\boldsymbol{\Psi}}^T\boldsymbol{x}_0$, thus omission of any of the modes in the modal basis will result in a difference in the initial conditions. The effect of the absence of modes on the initial condition can be accounted for by quasi–static correction or, mode acceleration, which is implemented in Ref. [21]. This work does not implement the quasi–static correction as the main interest is in excitation by external disturbance where the initial conditions will be zero.

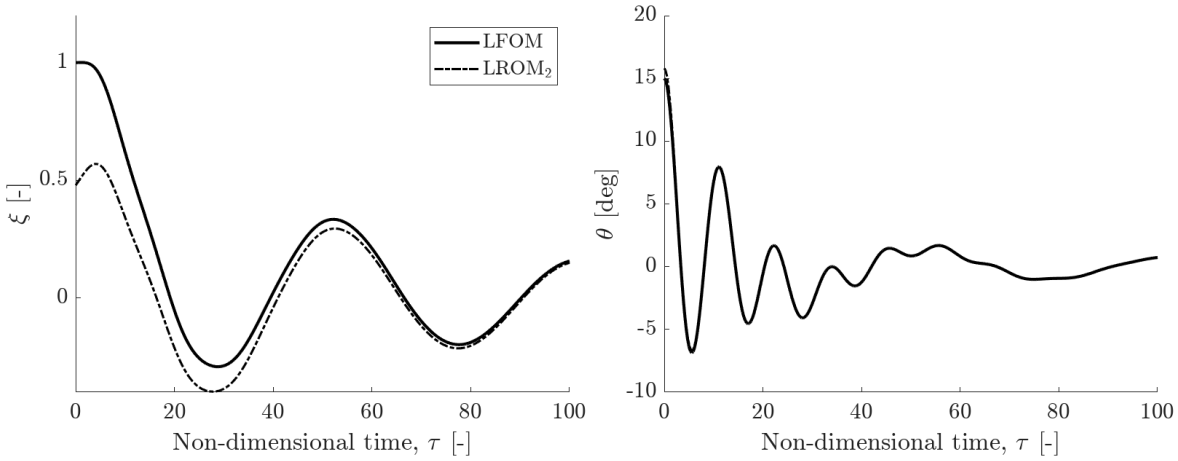

(a) Non–dimensional plunge (b) Pitch

Figure 13: Linear ROM dynamics due to initial condition perturbation.

The results shown in Figure 13 indicate that the free–response of the linear system may be adequately captured with a small subset of aeroelastic eigenvectors. Selecting only the modes relating to the decoupled structural system yields a respectably accurate approximation.

Analysis proceeds with a study of the linear dynamic response due to gust disturbance. As it is of interest to capture the dynamic response due to gust disturbance, the lowest frequency gust mode is added to the LROM_2 modal basis. This LROM is referred to as LROM_3. A discrete one–minus–cosine gust with gust gradient of $150\ ft$ is used to excite the dynamics of the linear FOM, LROM_2 and LROM_3. The effect of the introduction of this gust mode is seen in Figure 14. LROM_2 poorly captures the dynamics in non–dimensional plunge during the period of gust excitation. LROM_3 provides a better approximation of these dynamics, correcting the response during the period of excitation.

The aeroelastic system has two gust modes. Each gust mode corresponds to a state responsible for the aerodynamic contributions due to gust disturbances. It is found that the exact prediction of each gust state in the aeroelastic system is possible using only each state's corresponding gust mode. Therefore, by including both gust modes, one can obtain the exact contribution in lift coefficient due to gust disturbance. It is found though that introducing the highest frequency gust mode to the basis does not yield noticeable improvements in the quality of the dynamic response prediction. Analysis proceeds using only the lowest frequency gust mode.

Introduction of further aeroelastic modes provides incremental improvements to the quality of the approximation. Adding the highly damped torsional mode (Torsion*) to the modal basis provides some correction to the dynamics in pitch displacement during the period of gust excitation. This is shown as LROM_4 in Figure 14.

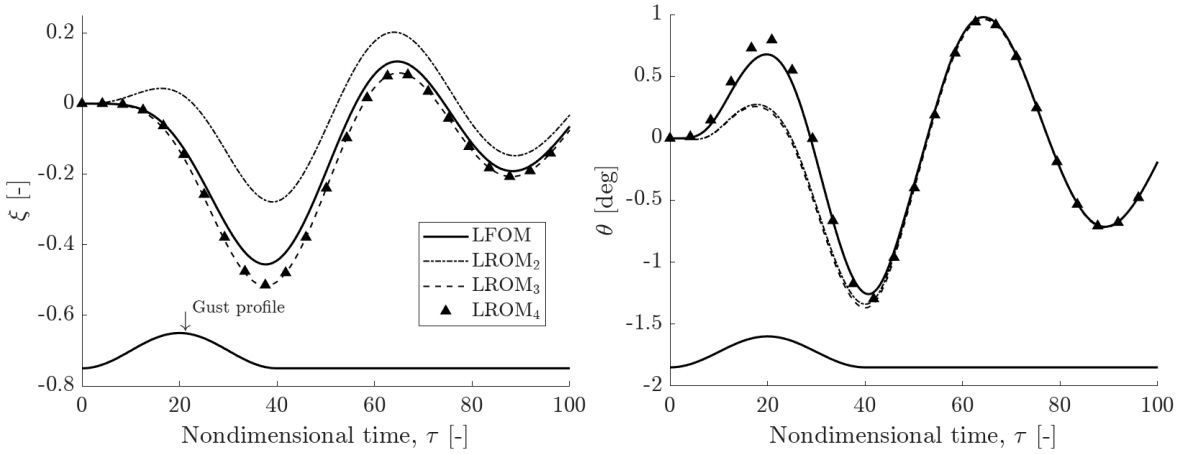

(a) Non–dimensional plunge (b) Pitch

Figure 14: Linear ROM and FOM dynamics in response to gust excitation.

Two further linear ROMs are considered and their dynamics shown in Figure 15. LROM$_6$ adds the two least damped aerodynamic modes to the basis. These are the lowest frequency circulatory indicial lift mode, and the circulatory indicial pitching moment due to step changes in pitch rate mode. It is seen in Figure 15 that introducing these two low frequency circulatory aerodynamic modes corrects the dynamic response in non–dimensional plunge, giving a near exact match with the linear FOM. The final LROM considered is LROM$_7$. This 7–mode LROM adds the instantaneous indicial lift due to step changes in angle of attack mode to the LROM$_6$ modal basis. LROM$_7$ captures the near exact dynamic response of the linear FOM in both non–dimensional plunge and pitch.

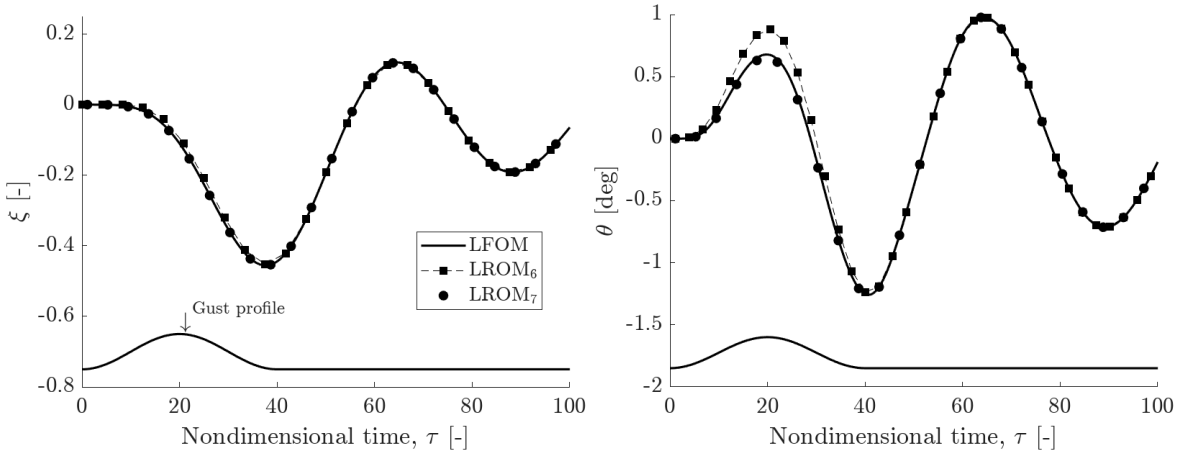

(a) Non–dimensional plunge (b) Pitch

Figure 15: Linear ROM and FOM dynamics in response to gust excitation.

The LROM$_7$ basis represents a truncation of high frequency aerodynamic content where it is noted those modes with frequency greater than $10\,Hz$ have been omitted. Furthermore, it is found that for aerodynamic contributions represented by a two–pole exponential, only the mode relating to the lowest frequency of the two poles is required. Specifically, only the lowest frequency circulatory indicial lift mode, and only the lowest frequency gust mode were required.

A worst–case gust search is now performed using the linear FOM and two linear ROMs. LROM_3 and LROM_7 are selected. These linear ROMs represent opposite extremes in terms of mode selection. At one extreme, minimisation of the modal basis to result in LROM dynamics which are at most characteristic of the LFOM, and at the other extreme, a more balanced minimisation of point by point error and modal basis size.

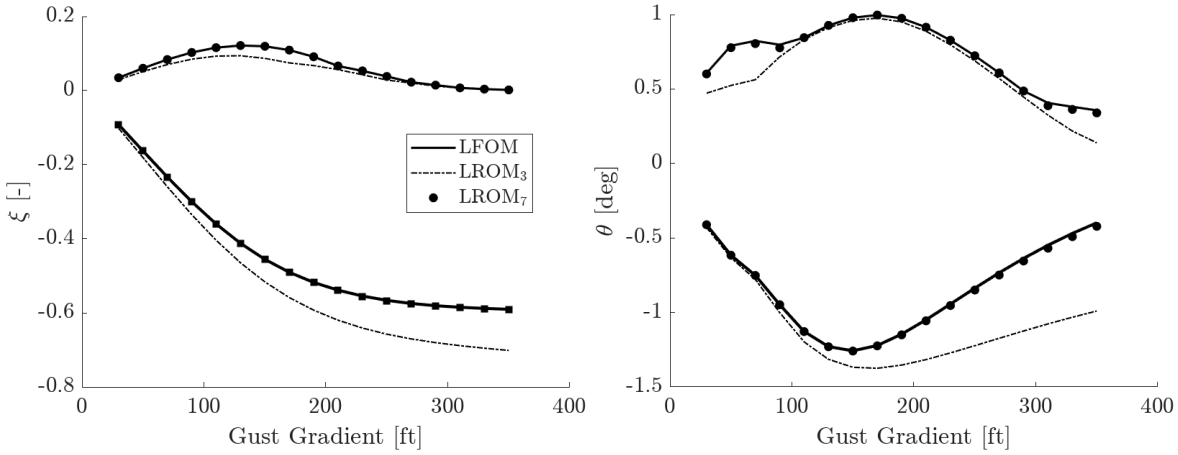

(a) Non–dimensional plunge

(b) Pitch

Figure 16: Maximum and minimum displacements of the linear FOM and ROM dynamical systems over increasing gust gradient.

It is seen in Figure 16 that across the entire range of gust gradients LROM_7 maintains a good match with the maximum and minimum displacements of plunge and pitch. LROM_3 however, is not as capable as LROM_7, and does not capture well the shape of the displacement profile across the gust gradient envelope. It is noted though that LROM_3 provides an adequate prediction of the peak maximum and minimum displacements, for example, at a gust gradient of $150\ ft$.

6.2 Nonlinear Aeroelastic Reduced Order Modelling

This work continues with discussion of nonlinear reduced order models of the dynamic aeroelastic system. Before proceeding, some commentary is provided on the form of the reduced order models.

The dynamics of the linear ROMs in the Section 6.1 were contained in the diagonal matrix, $\mathbf{\Lambda} \in \mathbb{C}^{m \times m}$. This matrix contained a subset of eigenvalues, which were obtained by solution of the eigenvalue problem of the aeroelastic system Jacobian matrix. Formation of the linear ROM systems does not require application of AD, and may be performed using commercially available eigenvalue solvers.

The aeroelastic system considered here contains second and third order nonlinearities in the structural system equations. Constructing a nonlinear reduced order model form then requires these second and third order nonlinearities expressed in the reduced order coordinate system. These nonlinear terms are obtained by use of source–transformation AD as discussed in Section 3.3. Reduced order nonlinear derivative functions for the second and third order terms are generated once from the full order source code, and parameterised with respect to the system properties given in Table 2, and the basis functions (eigenvectors). These reduced order higher derivative functions can be evaluated for any numerical value of those properties given in Table 2, and any given set of eigenvectors, at a fraction of the cost of generating the deriva-

tive functions. Evaluation of the higher derivative functions results in reduced order second derivative terms of dimension nm^2 and reduced order third derivative terms of dimension nm^3. Pre–multiplication of these derivatives by the conjugate transpose of the set of right eigenvectors results in the derivative dimensions being reduced to m^3 and m^4 respectively. This pre–multiplication is done outside of time–integration, which ensures computations using the nonlinear ROM system are performed only in the reduced dimension m.

The parameterisation of the reduced higher derivatives with respect to the basis functions is useful for a FOM of large dimension. Where it may be impractical by memory requirements to compute the full order third derivative of dimension n^4, providing a sufficiently small subset m of eigenvectors is chosen, the reduced order third derivative of dimension nm^3 will be less demanding by memory requirement. This work considers an already low dimensional FOM, where $n = 14$. Therefore the second and third reduced order derivative functions have been parameterised to retain all modes. The tensors resultant from evaluating these derivative functions are spliced where necessary to select a modal subset.

Discussion now proceeds with the analysis of the dynamics of the nonlinear reduced order model forms. The same modal bases as given in Table 4 are used for the nonlinear ROMs. These nonlinear ROMs are referred to as NROMs from hereon.

Figure 17 shows the dynamic response of NROM_2 compared with the NFOM. A pitch displacement of 15–degrees is used as the initial condition. It is seen that the effect of the structural nonlinearity on the dynamic response is captured by the ROM system. Specifically noting the nonlinear dynamics in non–dimensional plunge tending in the negative direction between 0 and 25 time units, while the linear dynamics tend in the positive direction as seen in Figure 8.

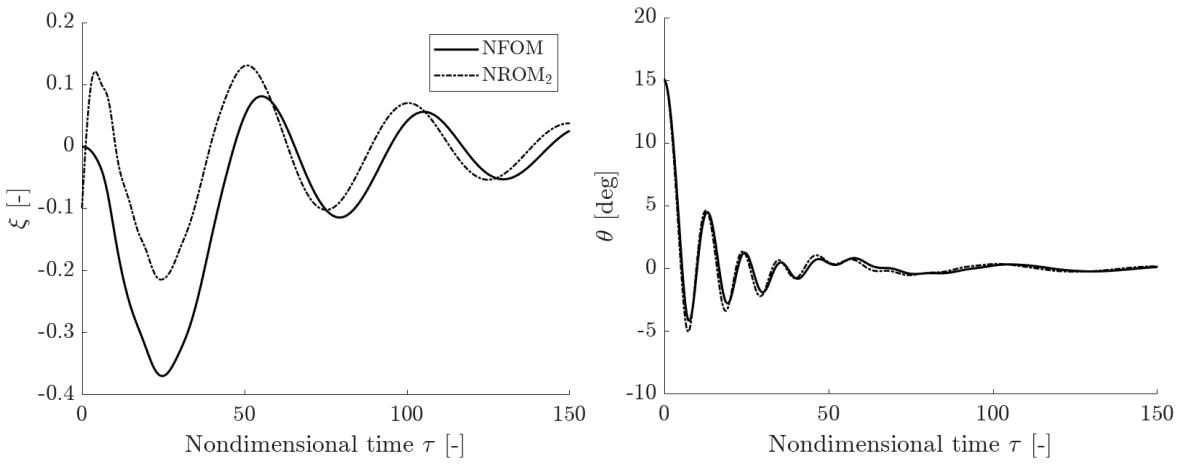

(a) Non–dimensional plunge (b) Pitch

Figure 17: Nonlinear ROM dynamics due to initial condition perturbation.

NROM_2 uses only the modes relating to bending and torsion in the decoupled fluid–structural system. As the FOM nonlinearity exists in the structural system, there is justification that the nonlinear ROM retaining only structural modes is able to capture some of this effect.

The nonlinear dynamic response due to gust disturbance is now considered. The dynamics are excited by a one–minus–cosine shaped gust, with gust gradient of $350\,ft$. This larger gust gradient is chosen as it ensures the dynamic response is sufficiently nonlinear, while being a

physically feasible gust excitation. The dynamic response of NROM_3 and NROM_4 are compared with the NFOM in Figure 18. It is seen that while both NROMs are able to capture the characteristic shape of the nonlinear dynamic response, neither are able to capture the peak displacements. It is noted though that the same trends in response prediction improvement are seen with NROM_3 and NROM_4 as were seen with LROM_3 and LROM_4. The addition of the highly damped torsional mode (Torsion*) provides some correction to the dynamic response during the period of gust disturbance.

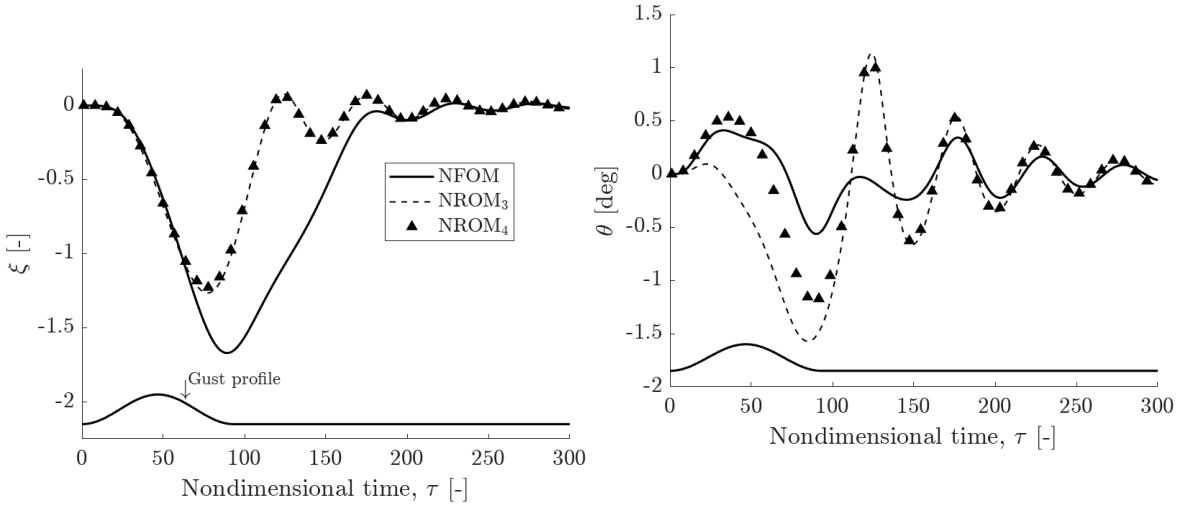

(a) Pitch

Figure 18: Nonlinear ROM and FOM dynamics in response to gust excitation.

The dynamics of NROM_6 and NROM_7 are shown in Figure 19. The addition of the two least damped circulatory aerodynamic modes in NROM_6 results in a significant improvement to the prediction quality. The dynamics of non–dimensional plunge displacement of NROM_6 are a near exact match with the nonlinear FOM. The addition of the instantaneous lift mode in NROM_7 finally results in the correction of the pitch dynamics. It is noted that the trends in the dynamic response corrections on adding modes to the nonlinear ROM bases are the same as with the linear ROM bases. This is a positive result, as it indicates that information obtained during the assembly of a linear ROM can be used to guide the assembly of a nonlinear ROM.

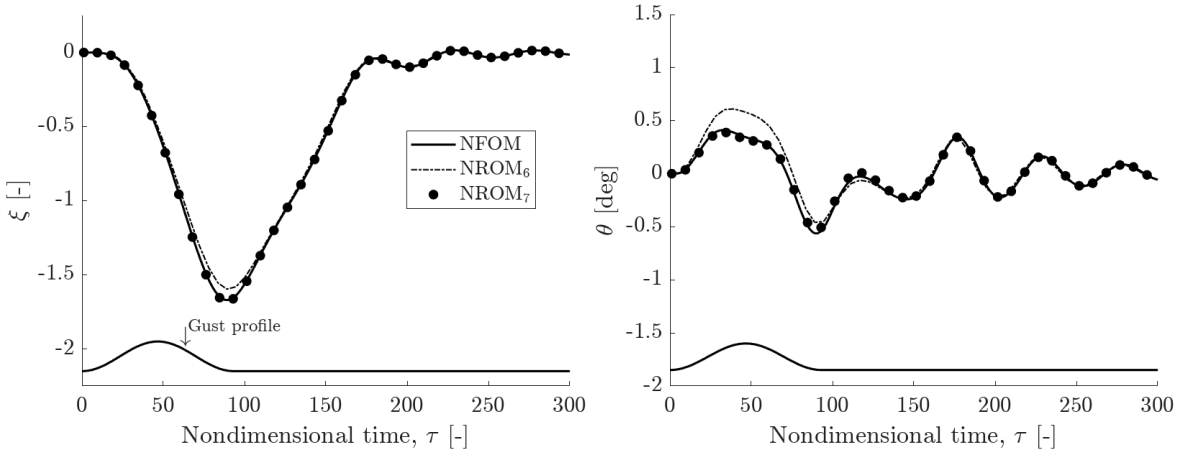

(a) Non–dimensional plunge (b) Pitch

Figure 19: Nonlinear ROM and FOM dynamics in response to gust excitation.

A worst–case gust search is performed with NROM_3, NROM_7 and the nonlinear FOM. The maximum and minimum displacements across a range of gust gradients is given in Figure 20. It is seen that while NROM_3 is able to capture the effect of the structural nonlinearity in plunge and pitch over the range of gust gradients, large errors are seen, specifically at the extremes of the gust gradient range. NROM_7 however performs well with near coincident results with the NFOM. NROM_7 maintains a small near constant error over a range of excitations, which is a desirable trait in a ROM.

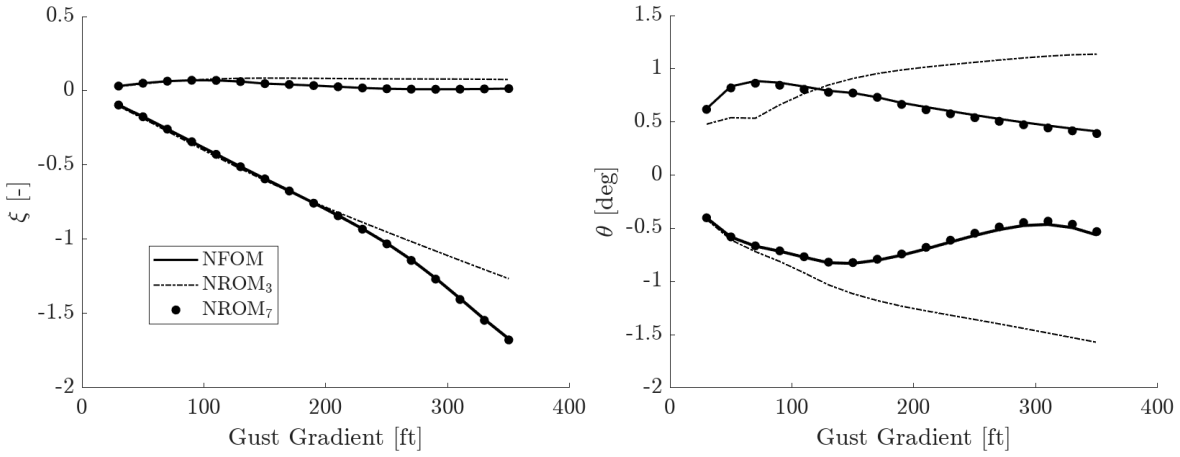

(a) Non–dimensional plunge

(b) Pitch

Figure 20: Maximum and minimum displacements of the nonlinear FOM and ROM dynamical systems over increasing gust gradient.

The final case considered in this work is the prediction of the nonlinear dynamic response in the post–flutter regime. The system is in equilibrium at $9,843\ ft$ at $M = 0.85$, which are the same conditions as the FOM post–flutter dynamics study in Section 5.4. It is found that a nonlinear ROM using a basis of only three modes is able to sufficiently capture the characteristic shape of the nonlinear dynamic response in the post flutter regime. These three modes include the two modes relating to the decoupled structural system in bending and torsion, and the least damped aerodynamic mode – which corresponds to circulatory indicial lift. Results for this three mode nonlinear ROM are shown in Figure 21, where a 15–degree perturbation in pitch displacement is used as the initial condition. It can be seen that the amplitude and period of the stable LCOs is captured well by the three mode nonlinear ROM.

7 CONCLUSIONS

This work has presented efforts towards the application of a parametric nonlinear model reduction architecture to aeroelastic dynamical systems. The present work has seen this architecture applied to a two–dimensional aerofoil system with up to cubic nonlinearities in the structural equations. Analysis of the nonlinear dynamics of the full model revealed that sufficient prediction of these dynamics is not possible using the linearised system, thus motivating the need for a nonlinear reduced model form.

The nonlinear model reduction method projects a Taylor series expansion of the full model onto a subset of eigenvectors which are representative of the dynamics of the full model. These eigenvectors were derived from the solution of the eigenvalue problem of the aeroelastic system Jacobian matrix. Aeroelastic mode tracking techniques were used to assist in assigning meaning to the aeroelastic modes. The basis of eigenvectors were identified as those that originated in

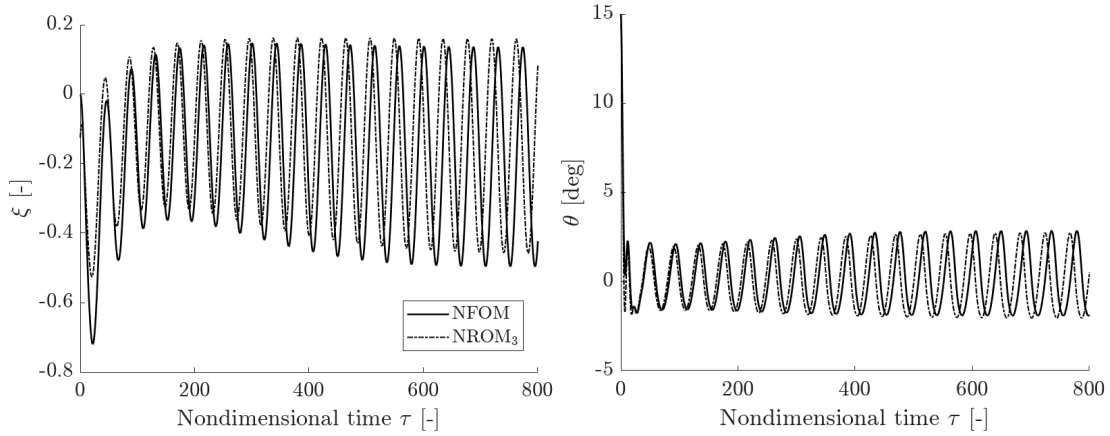

(a) Non–dimensional plunge (b) Pitch

Figure 21: Post–flutter nonlinear ROM and FOM dynamics in response to a 15 degree perturbation in pitch displacement in the initial conditions.

the decoupled structural system, and those that originated in the decoupled fluid system. Due to the form of the unsteady aerodynamic model, it was further possible to identify the physical aerodynamic state that specific aeroelastic modes corresponded to.

A linear ROM constructed using only 3 aeroelastic modes of the 14–state FOM was found to have adequate predictive capability of the linear dynamics due to gust disturbance. 7 modes were required to capture the near exact dynamic response of the FOM. The 7–mode ROM represented a truncation of high–frequency aerodynamic content.

Nonlinearities were retained by taking higher derivatives of the FOM dynamical system with respect to the ROM coordinate system. This was made possible by use of source–transformation automatic differentiation. Parametric, reduced order second and third derivative codes of the FOM code were generated. These codes could be evaluated for any set of system parameters at a fraction of the cost of the ROM code generation. Computing the second and third derivative ROM terms using the 7–mode basis resulted in a nonlinear ROM dynamical system able to capture the near exact dynamics of the nonlinear FOM over a range of gust disturbances. A smaller subset of 3 modes was found sufficient to predict LCOs in the post–flutter regime.

Future work will see to the application of this method in control law design for nonlinear aeroelastic systems. The form and structure of these nonlinear ROMs is highly applicable to control law design where computational complexity and model size should be minimal.

8 REFERENCES

[1] Da Ronch, A., Badcock, K. J., Wang, Y., et al. (2012). Nonlinear Model Reduction for Flexible Aircraft Control Design. In *American Institute or Aeronautics and Astronautics Flight Mechanics Conference*.

[2] Massegur, D., Clifford, D., Da Ronch, A., et al. (2022). Comparing reduced order models for nonlinear dynamical systems. In *ICAS 2022: Computational Aeroelasticity*.

[3] Da Ronch, A., Tantaroudas, N. D., Timme, S., et al. (2013). Model Reduction for Linear and Nonlinear Gust Loads Analysis. Tech. rep., University of Southampton, Southampton.

[4] Tantaroudas, N. D. and Da Ronch, A. (2017). Nonlinear Reduced-order Aeroservoelastic Analysis of Very Flexible Aircraft. In A. Da Ronch and P. Marqués (Eds.), *Advanced UAV Aerodynamics, Flight Stability and Control*, chap. 4. Chichester: Wiley, first edition ed., pp. 143–180.

[5] Patterson, M. A., Weinstein, M., and Rao, A. V. (2013). An Efficient Overloaded Method for Computing Derivatives of Mathematical Functions in MATLAB. *ACM Transactions on Mathematical Software*, 39(3). ISSN 23103582. doi:10.1145/0000000.0000000.

[6] Bisplinghoff, R., Ashley, H., and Halfman, R. (1996). *Aeroelasticity*. Toronto: General Publishing Company, dover edition ed.

[7] Lee, B. H. K., Price, S. J., and Wong, Y. S. (1999). Nonlinear aeroelastic analysis of airfoils: bifurcation and chaos. *Progress in Aerospace Sciences*, 35, 205–334.

[8] Lee, B. H. K., Jiang, L. Y., and Wong, Y. S. (1999). Flutter of an airfoil with a cubic restoring force. *Journal of Fluids and Structures*, 13.

[9] Leishman, J. G. and Nguyen, K. Q. (1990). State-space representation of unsteady airfoil behavior. *AIAA Journal*, 28(5), 836–844. ISSN 00011452. doi:10.2514/3.25127.

[10] Wagner, H. (1925). Uber die Entstehung des dynamischen Auftriebes von Tragflugeln. *Zeitschrift fur Angewandte Mathematic und Mechanik*.

[11] Jones and Robert, T. (1940). The Unsteady Lift of a Wing of Finite Aspect Ratio. NACA Rep. 681.

[12] Theodorsen, T. (1935). General Theory of Aerodynamic Instability and the Mechanism of Flutter.

[13] Mazelsky, B. (1951). Numerical Determination of Indicial Lift of a Two-Dimensional Sinking Airfoil at Subsonic Mach Numbers from Oscillatory Lift Coefficients with Calculations for Mach Number 0.7.

[14] Leishman, J. (1993). Indicial lift approximations for two-dimensional subsonic flow as obtained from oscillatory measurements. *Journal of Aircraft*, 30, 340–351.

[15] Leishman, J. G. (1996). Subsonic unsteady aerodynamics caused by gusts using the indicial method. *Journal of Aircraft*, 33(5), 869–879. ISSN 15333868. doi:10.2514/3.47029.

[16] Leishman, J. G. (1993). Indicial lift approximations for two-dimensional subsonic flow as obtained from oscillatory measurements. *Journal of Aircraft*, 30(3), 340–351. ISSN 00218669. doi:10.2514/3.46340.

[17] Crouse, G. L. and Leishman, J. G. (1992). Transonic aeroelasticity analysis using state-space unsteady aerodynamic modeling. *Journal of Aircraft*, 29(1), 153–160. ISSN 00218669. doi:10.2514/3.46139.

[18] Mallik, W. and Kapania, R. (2018). Rapid Transonic Flutter Analysis for Aircraft Conceptual Design Applications. *AIAA Journal*, 56(6).

[19] Hang, X., Fei, Q., and Su, W. (2019). On tracking aeroelastic modes in stability analysis using left and right eigenvectors. *AIAA Journal*, 57(10), 4447–4457. ISSN 00011452. doi:10.2514/1.J057297.

[20] US Federal Aviation Administration (2014). Advisory Circular No 25.341-1 – Dynamic Gust Loads.

[21] Romanowski, M. C., Dowell, E. H., and Laursen, S. G. S. (1995). *Using fluid eigenmodes to develop euler based reduced order unsteady aerodynamic and aeroelastic models.* Ph.D. thesis, Duke University, Durham.

COPYRIGHT STATEMENT